Ocean Color Algorithm for the Retrieval of the Particle Size Distribution and Carbon-Based Phytoplankton Size Classes Using a Two-Component Coated-Spheres Backscattering Model

Tihomir S. Kostadinov[1], Lisl Robertson Lain[2], Christina Eunjin Kong[3], Xiaodong Zhang[4], Stéphane Maritorena[5], Stewart Bernard[6], Hubert Loisel[7], Daniel S.F. Jorge[8], Ekaterina Kochetkova[9], Shovonlal Roy[10], Bror Jonsson[11], Victor Martinez-Vicente[12], and Shubha Sathyendranath[13]

[1]Department of Liberal Studies, California State University San Marcos, 333 S. Twin Oaks Valley Rd., San Marcos, CA 92096, USA

[2]Earth Observation, Smart Places, CSIR; formerly with University of Cape Town, Department of Oceanography, Cape Town, South Africa

[4]Division of Marine Science, School of Ocean Science and Engineering, The University of Southern Mississippi, Stennis Space Center, MS 39529, USA

[5]Earth Research Institute, University of California at Santa Barbara, Santa Barbara, CA 93106-3060, USA

[6]SANSA, Enterprise Building, Mark Shuttleworth Street, Innovation Hub, Pretoria 0087, South Africa

[7,8]Laboratoire d'Océanologie et de Géosciences, Université du Littoral-Côte-d'Opale, Université Lille, CNRS, IRD, UMR 8187, LOG, 32 avenue Foch, Wimereux, France

[9]Department of Earth & Environmental Science, Hayden Hall, University of Pennsylvania, 240 South 33rd St., Philadelphia, PA 19104, USA

[10]Department of Geography and Environmental Science, University of Reading, Reading, United Kingdom

[3,11,12,13]National Centre for Earth Observation, Plymouth Marine Laboratory, UK

Correspondence: Tihomir S. Kostadinov (tkostadinov@csusm.edu)

Abstract. The particle size distribution (PSD) of suspended particles in near-surface seawater is a key property linking biogeochemical and ecosystem characteristics with optical properties that affect ocean color remote sensing. Phytoplankton size affects their physiological characteristics and ecosystem and biogeochemical roles, e.g. in the biological carbon pump, which has an important role in the global carbon cycle and thus climate. It is thus important to develop capabilities for measurement and predictive understanding of the structure and function of oceanic ecosystems, including the PSD, phytoplankton size classes (PSCs) and phytoplankton functional types (PFTs). Here, we present an ocean color satellite algorithm for the retrieval of the parameters of an assumed power-law PSD. The forward optical model considers two distinct particle populations (particle assemblage categories) — phytoplankton and non-algal particles (NAP). Phytoplankton are modeled as coated spheres following the Equivalent Algal Populations (EAP) framework, and NAP are modeled as homogeneous spheres. The forward model uses Mie and Aden-Kerker scattering computations, for homogeneous and coated spheres (for phytoplankton and NAP, respectively), respectively, to model the total particulate spectral backscattering coefficient as the sum of phytoplankton and NAP backscattering. The PSD retrieval is achieved via Spectral Angle Mapping (SAM) which uses backscattering endmembers created by the forward model. The PSD is used to retrieve size-partitioned absolute and fractional phytoplankton carbon concentrations (i.e. carbon-based PSCs), as well as particulate organic carbon (POC), using allometric coefficients. The EAP-based formulation allows for This model formulation also allows the estimation of chlorophyll-a concentration via the

retrieved PSD, as well as ~~the estimation of the~~ percent of backscattering due to NAP vs. phytoplankton. The PSD algorithm is operationally applied to the merged Ocean Colour Climate Change Initiative (OC-CCI) v5.0 ocean color data set. Results of an initial validation effort are also presented, using PSD, POC, and pico-phytoplankton carbon *in-situ* measurements. Validation results indicate the need for an empirical tuning for the absolute phytoplankton carbon concentrations; however these results and comparison with other phytoplankton carbon algorithms are ambiguous as to the need for the tuning. The latter finding illustrates the continued need for high-quality, consistent, large global data sets of PSD, phytoplankton carbon and related variables to facilitate future algorithm improvements.

1 Introduction

Oxygenic photosynthesis by marine phytoplankton is a critical planetary scale process supplying solar energy to the biosphere by fixing inorganic carbon; it is responsible for roughly half of global annual net primary productivity (e.g. Field et al. (1998)). Ocean ecosystems play a key role in Earth's carbon cycle and climate by affecting atmospheric CO_2 via the biological carbon pump, which sequesters some of the fixed carbon to the deeper ocean for longer time scales (e.g. Eppley and Peterson (1979); Chisholm (2000); Henson et al. (2011); Boyd et al. (2019); Brewin et al. (2021)). The biological pump is influenced by the structure and function of oceanic ecosystems (e.g. Falkowski et al. (1998); Siegel et al. (2014)); therefore, mechanistic, predictive understanding of ocean ecosystems is of high priority to Earth systems and climate research (e.g. Buesseler and Boyd (2009); Siegel et al. (2016)). Satellite remote sensing of ocean color is a key tool for the global characterization of ocean ecology (e.g. Siegel et al. (2013)). This has led to large efforts to elucidate biological pump mechanisms using multiple platforms, including satellites, e.g. the EXPORTS Program (Siegel et al., 2016).

Phytoplankton cell size (diameters varying from ≈ 0.5 µm to > 50 µm (e.g. Clavano et al. (2007)) is ~~an important~~ a key trait that affects multiple phytoplankton characteristics (Marañón (2015)), as well as sinking rates (e.g. Falkowski et al. (1998); Burd and Jackson (2009); Stemmann and Boss (2012); Siegel et al. (2014)). Phytoplankton size classes (PSCs) thus tend to closely correspond to phytoplankton functional types (PFTs, e.g., Quéré et al. (2005)). Importantly, phytoplankton cells also affect the inherent optical properties (IOPs) (e.g. absorption and backscattering coefficients) of the water column in a size-dependent manner (e.g. Mobley et al. (2002); Morel and Bricaud (1986); Stramski and Kiefer (1991); Kostadinov et al. (2009)). This is because particle size (relative to the incident light wavelength) is one of the governing variables affecting the magnitude and spectral shape of light scattering and absorption caused by a particle (e.g. Bohren and Huffman (1983)). Therefore the particle size distribution (PSD) of phytoplankton (and other suspended particles in seawater) is a key property affecting both optical properties and cellular physiological and biogeochemical properties, i.e. it is a fundamental property linking ocean color remote sensing and ecosystem/biogeochemical characteristics. The size distribution of particles suspended in near surface ocean waters is often described as a power law, given in differential form as follows (e.g. Bader (1970); Sheldon et al. (1972); Jonasz (1983); Boss et al. (2001); Twardowski et al. (2001); Kostadinov et al. (2009); Roy et al. (2017)):

$$\frac{dN_T}{dD} = N(D) = N_0 \left(\frac{D}{D_0} \right)^{-\xi} \tag{1}$$

where D is particle diameter, N [m^{-4}] is the differential number concentration of particles per unit volume seawater and per bin width of particle diameter, $N_0 = N(2\,\mu m)$ is the particle number concentration at a reference diameter, here $D_0 = 2$

50 µm, ~~D is particle diameter,~~ and ξ is the power-law slope of the PSD. Equation 1 has to be integrated over a given diameter range to get the total ~~volumetric particle~~ particle number concentration in that range, N_T, [m^{-3}].

Ocean color is quantified by the spectral shape and magnitude of the remote-sensing reflectance, $R_{rs}(\lambda)$ [sr^{-1}], where λ is the wavelength of light *in vacuo*. The Kostadinov-Siegel-Maritorena 2009 (KSM09, Kostadinov et al. (2009)) algorithm retrieves the parameters of an assumed power-law PSD (ξ and N_0 in Eq. 1) from ocean color remote-sensing observations, using

55 the spectral shape (Loisel et al., 2006) and magnitude of the particulate backscattering coefficient, $b_{bp}(\lambda)$ [m^{-1}]. $b_{bp}(\lambda)$ can be retrieved using existing inherent optical property (IOP) inversion algorithms; KSM09 uses the Loisel and Stramski (2000) IOP inversion. Subsequently, the retrieved PSD parameters allow the quantification of absolute and fractional PSCs — picoplankton, nanoplankton and microplankton, based on bio-volume (Kostadinov et al., 2010) or phytoplankton carbon (Kostadinov et al., 2016a) (henceforth TK16) via allometric relationships (Menden-Deuer and Lessard, 2000). Phytoplankton carbon (phyto C)

60 is the key variable of interest for carbon cycle and climate studies and modeling, and TK16 (data set available — Kostadinov et al. (2016b)) represents a relatively unique carbon-based approach among PSC/PFT algorithms (Mouw et al., 2017) as it is based on knowledge of the PSD and allometric relationships to get at size-partitioned phyto C. Roy et al. (2013, 2017) retrieve phytoplankton-specific PSD and size-partitioned phyto C, based on the phytoplankton absorption coefficient.

The KSM09 PSD algorithm (and the TK16 phyto C/PSC derived from it) is built on the assumption of a single population of

65 particles (approximated by homogeneous spheres), representing backscattering due to the entire oceanic particle assemblage — phytoplankton cells and non-algal particles (NAP). However, particle internal composition and shape influence its optical properties (e.g Quirantes and Bernard (2004, 2006)). Recent results suggest that the structural complexity of oceanic particles enhances backscattering significantly and can explain the so-called "missing backscattering" in the ocean (Organelli et al., 2018), i.e. the lack of optical closure between theoretically modeled and measured b_{bp}. Coated spheres (i.e. spheres consisting

70 of concentric layers/shells of different material properties) can be used to better represent phytoplankton cells and their internal heterogeneity and composition (e.g. Bernard et al. (2009); Robertson Lain and Bernard (2018)), and they have significantly enhanced backscattering compared to their homogeneous equivalents (Duforêt-Gaurier et al., 2018; Organelli et al., 2018).

Here, we introduce a major improvement of the ~~KSM09 PSD algorithm~~ PSD algorithm formulation. Two separate particle populations are modeled, living phytoplankton cells and NAP. Phytoplankton cells are modeled as coated spheres, following

75 the Equivalent Algal Populations (EAP) framework (Bernard et al., 2009; Robertson Lain et al., 2014; Robertson Lain and Bernard, 2018). EAP explicitly models intracellular chlorophyll concentration, Chl_i, as governing the imaginary index of refraction, and thus allows for bulk chlorophyll concentration (Chl) to be computed from a specific PSD. The coated sphere EAP-based model is useful to better represent specifically phytoplankton cells; however, not all backscattering particles are phytoplankton (Stramski et al., 2004), and in fact, sub-micron NAP even smaller than the smallest autotroph ($\approx 0.5\,\mu m$ in

80 diameter) are critical for determining the spectral shape of b_{bp}, which is key for PSD retrieval with KSM09 and the algorithm presented here. Particles other than and smaller than phytoplankton are likely to significantly contribute to backscattering (Stramski et al., 2004; Zhang et al., 2020), in spite of evidence that phytoplankton/larger particles contribute more than Mie

theory predicts, based on homogeneous spheres (e.g. Dall'Olmo et al. (2009)). Thus, a 2-component particle model is used here, separately modeling NAP as homogeneous spheres of wider size range than phytoplankton, so that bulk b_{bp} of oceanic waters can be modeled (e.g. Stramski et al. (2001); Moutier et al. (2016); Duforêt-Gaurier et al. (2018)). NAP are modeled as having generally organic detrital composition, but with some allowance for higher indices of refraction to account for minerogenic particle contributions. The PSD forward model can thus also produce a first-order estimate of POC, and the percent contribution of phytoplankton and NAP to b_{bp}.

Subsequent sections present details of the 2-component, EAP-based forward IOP model, the inversion methodology developed for operational application of the PSD algorithm, and the ~~subsequent~~ use of the satellite-derived PSD to retrieve derived products (following the methods of TK16 with some modifications), namely - absolute and fractional size-partitioned phytoplankton carbon (henceforth phyto C) (i.e. carbon-based PSCs), as well as Chl and POC estimates. The novel algorithm is applied operationally to monthly data from the multi-sensor merged OC-CCI v5.0 data set (Sathyendranath et al., 2019, 2021) — examples are shown in the manuscript, and the entire data set is publicly available and linked below (See Sec. 4). We then present and discuss an initial effort of validation of the new PSD algorithm and derived products using global compilations of PSD, pico-phytoplankton carbon and POC in-situ data. A comparison with other existing methods to retrieve phyto C is presented. We also discuss algorithm uncertainties, assumptions and limitations as well as future work directions.

2 Data and Methods

2.1 Particle optical model input specification for Phytoplankton and NAP

The contributions of two separate particle populations to bulk backscattering are modeled using Mie theory (Mie, 1908) for homogeneous spherical particles and the Aden-Kerker (Aden and Kerker, 1951) method for coated spheres. Living phytoplankton cells are represented by the first particle population, and all other suspended particles of any origin (i.e. ~~non-algal particles,~~ NAP) are represented by the second population. Living phytoplankton cells are modeled as coated spheres using the Equivalent Algal Populations (EAP) framework (Bernard et al., 2009; Robertson Lain et al., 2014; Robertson Lain and Bernard, 2018) for determining optical model inputs, in particular the complex indices of refraction of the particle core and coat. NAP are modeled as homogeneous spheres meant to represent organic detritus, but also allowing for their real index of refraction to vary over a wider range to take into account the contribution of mineral particles.

A characteristic of the PSD algorithm presented here is that it is mechanistic to the extent feasible, i.e. based on first principles and causality, even at the expense of increasing complexity. For example, as in EAP, the imaginary refractive index (RI) of the cell is a function of intracellular chlorophyll concentration, Chl_i. ~~Importantly, here we~~ We vary some optical model inputs in a Monte Carlo simulation in order to assess uncertainty and base the PSD inversion on an ensemble of forward runs rather than a single ~~specific~~ set of inputs. Details of uncertainty estimation and propagation are given in Supplement Sec. S1. Details of how each input parameter for phytoplankton cells and for NAP is specified, as well as the statistical distributions from which the Monte Carlo simulation instances were picked are specified in Table 1 and Table 2.

As in the EAP model, the chloroplast is represented by the particle coat. Its relative volume, V_s, is picked from a distribution as shown in Table 1. The chloroplast's imaginary refractive index (RI) (relative to seawater) at 675 nm, $n'(675)$, is then computed as follows (Morel and Bricaud, 1986; Bernard et al., 2009; Robertson Lain and Bernard, 2018):

$$n'(675) = \frac{Chl^* \times Chl_i \times 10^6 \times 675 \times 10^{-9}}{4\pi \times V_s \times n_{sw}(675)} \tag{2}$$

where Chl^* = 0.027 m^2mg^{-1} is the theoretical maximum specific absorption coefficient of chlorophyll at 675 nm when dissolved in water (Bernard et al., 2009; Robertson Lain and Bernard, 2018), Chl_i is the intracellular chlorophyll concentration in kg Chl m^{-3} of cellular material, and $n_{sw}(675)$ is seawater's absolute real RI at 675 nm. A hyperspectral basis vector from the EAP model (based on measurements, for details see Bernard et al. (2009); Robertson Lain and Bernard (2018)) is then scaled using the value at 675 from Eq. 2, obtaining a hyperspectral relative imaginary RI for the coat as chloroplast. In Eq. 2, Chl_i applies to the whole cell and is therefore scaled using V_s to obtain $n'(675)$ for the coat alone. The nominal chloroplast's real relative RI is then picked from a distribution as shown in Table 1, and modified as a function of its imaginary RI according to the Kramers-Kronig relations (implemented as a Hilbert transform) (Bernard et al., 2009; Robertson Lain and Bernard, 2018).

The cell cytoplasm is represented by the particle core. It's real relative RI is picked from a distribution given in Table 1, and it is modified by the Kramers-Kronig relations using a constant hyperspectral detritus-like imaginary RI, i.e. having a colored dissolved organic matter (CDOM)-like exponential spectral shape, resulting in spectrally-varying hyperspectral relative real RI. The phytoplankton particle population relative RIs and their Monte Carlo variability are summarized in Supplement Fig. S1.

The NAP population is represented by a homogeneous sphere, the relative RIs of which are picked so that its absorption spectrum is detritus-like (same as the core of phytoplankton), and its real RI is allowed to vary over a wider range of values, meant to represent mostly organic detritus, but with some minerogenic contributions, resulting in a mean nominal real relative RI of ≈ 1.06. The input RIs and other input parameters for NAP are summarized in Table 2.

Specification of the input PSD parameters and the relationship of NAP to phytoplankton PSDs is key to the construction of the forward and inverse models. Necessarily, some key simplifying assumptions are made here in order to construct an algorithm with operational application to modern multi-spectral ocean color sensors. The two key assumptions are: 1) Phytoplankton and NAP have a power-law PSD (Eq. 1) with the same slope ξ, and 2) The scaling parameter N_0 for NAP is twice that of N_0 for phytoplankton (the forward model uses default values as in Tables 1 and 2). The latter assumption is chosen so that it results in a phyto C:POC ratio of 1:3 (see Kostadinov et al. (2016a) and Behrenfeld et al. (2005), and Sec. 3.4 here) (as long as they are both estimated using the same size ranges). Together, these assumptions allow for the retrieval of one common PSD parameter set pertaining to the total particle population PSD (one ξ value and one total N_0 equal to the linear sum of the NAP and phytoplankton N_0 values).

Input Parameter	Symbol, Units & Notes
Pure Seawater Absolute Real RI	$n_{sw} = f(\lambda)$, after Zhang et al. (2009) using Temperature = 15 °C & Salinity = 33
PSD slope	$\xi \in [2.5, 6]$ in steps of 0.05. The same value applies to both phytoplankton and NAP. For the slope range, see, e.g. Boss et al. (2001)
Wavelengths *in vacuo*	$\lambda \in [400, 700]$ nm; hyperspectral - in steps of 1 nm. Band-averaging used for the nominal wavelengths of satellite sensors.
Phytoplankton Population Inputs	
Intracellular Chlorophyll Concentration	$Chl_i \in [0.5, 10]$, picked from, $\mathcal{N}(2.5, 2.5)$; $\mu \approx 3.14$ kg Chl m^{-3} cellular material (Morel and Bricaud (1986); Bernard et al. (2009)).
Coat (Chloroplast) Relative Volume	$V_s \in [5, 35]$ %, picked from $\mathcal{N}(20, 5)$, resulting in mean coat relative thickness as fraction of cell radius $t_{coat} = 7.2\%$ (cf. Organelli et al. (2018)); $t_{coat} = 1 - (1 - V_s)^{1/3}$
Coat (Chloroplast) Relative Real RI	$n_{coat} \in [1.06, 1.22]$, picked from, $\mathcal{N}(1.14, 0.08)$; $\mu \approx 1.14$; wavelength-dependent via Kramers-Kronig relations (Bernard et al. (2009); Robertson Lain and Bernard (2018)).
Core (cytoplasm) Relative Real RI	$n_{core} \in [1.01, 1.03]$, picked from, $\mathcal{N}(1.02, 0.01)$; $\mu \approx 1.02$; wavelength-dependent via Kramers-Kronig relations (Bernard et al. (2009); Robertson Lain and Bernard (2018)).
Coat (Chloroplast) Relative Imaginary RI	$n'_{coat}(\lambda)$ is computed from a hyperspectral basis vector (from Bernard et al. (2009); Robertson Lain and Bernard (2018)) that is scaled to the value at $n'(675)$ using Eq. 2.
Core (cytoplasm) Relative Imaginary RI	$n'_{core}(\lambda)$ has a prescribed constant magnitude & detritus-like (exponential) spectral shape, with spectral slope $S = 0.0123$ nm^{-1}, resulting in $S_a \approx 0.014$ nm^{-1} for $a_{core}(\lambda)$ (Bernard et al. (2009); Robertson Lain and Bernard (2018)).
Minimum outer particle diameter	$D_{min_\phi} = 0.5$ µm (smallest autotroph e.g. Morel et al. (1993))
Maximum outer particle diameter	$D_{max_\phi} \in [20, 200]$ µm, picked from, $\mathcal{N}(50, 50)$; $\mu \approx 72.3$ µm;
Differential Number Concentration at $D_0 = 2$ µm	$N_{0\phi} = 5 \times 10^{16}$ m^{-4}. Used in the forward modeling.

Table 1. Inputs for the coated spheres Aden-Kerker optical scattering computations for the phytoplankton particle population. Modeling inputs common to both phytoplankton and NAP (see Table 2) are given in the first three table rows. $\mathcal{N}(\mu, \sigma)$ stands for a normal distribution with mean μ and standard deviation σ. For the indices of refraction, apart from Bernard et al. (2009); Robertson Lain and Bernard (2018), see Morel and Bricaud (1986); Babin et al. (2003); Woźniak and Stramski (2004); Duforêt-Gaurier et al. (2018)

NAP Population Inputs	
Relative Real RI	$n_{NAP} \in$ [1.01, 1.2], picked from, $\mathcal{N}(1.02,0.06)$; $\mu \approx$ 1.06; wavelength-dependent via Kramers-Kronig relations. (Bernard et al. (2009); Robertson Lain and Bernard (2018))
Relative Imaginary RI	$n'_{NAP}(\lambda)$ has a prescribed constant magnitude & detritus-like (exponential) spectral shape (Bernard et al. (2009); Robertson Lain and Bernard (2018)), with spectral slope $S = 0.0123$ nm^{-1}, resulting in $S_a \approx 0.014$ nm^{-1} for $a_{NAP}(\lambda)$.
Minimum ~~outer~~ particle diameter	$D_{min\,NAP} = 0.01$ µm (See Supplement Fig. S4 and Stramski and Kiefer (1991); Kostadinov et al. (2009)
Maximum ~~outer~~ particle diameter	$D_{max\,NAP} \in$ [200, 500] µm (e.g. Duforêt-Gaurier et al. (2018)), picked from, $\mathcal{N}(400,10)$; $\mu \approx 376.8$ µm;
Differential Number Concentration at $D_0 = 2$ µm	$N_{0\,NAP} = 2 \times N_{0\phi} = 1.0 \times 10^{17}$ m^{-4}, resulting in total particle population $N_0 = 1.5 \times 10^{17}$ m^{-4}. Used in the forward modeling. $N_{0\,NAP} = 2 \times N_{0\phi}$ constitutes an important model assumption and it is discussed in the text.

Table 2. Inputs for the homogeneous spheres Mie scattering code for the NAP population. Modeling inputs common to both phytoplankton and NAP are given in the first three table rows of Table 1. $\mathcal{N}(\mu, \sigma)$ stands for a normal distribution with mean μ and standard deviation σ.

2.2 Backscattering Calculations

The backscattering efficiencies $Q_{bb}(\lambda)$, for a single phytoplankton cell and NAP particle were computed using ~~using~~ the inputs described above in Sec. 2.1 and Tables 1 and 2. The coated spheres code of Zhang et al. (2002) was used for both coated and homogeneous spheres. This code is included with the algorithm development scientific code of the PSD algorithm (see Sec. 4).

150 Calculations were run for N = 3000 instances of Monte Carlo simulations, each with a unique randomly picked combination of inputs for phytoplankton and NAP. This resulted in 3000 sets of hyperspectral Q_{bb} values. High sampling resolution in diameter space was picked for the coated spheres (10000 samples between minimum and maximum diameter) in order to minimize the influence of resonance spikes in Q_{bb}. For NAP, 1000 samples of D were used.

Indices of refraction for both phytoplankton and NAP are specified hyperspectrally (Supplement Fig. S1) and the computa-

155 tions are performed from 400 nm to 700 nm wavelength *in vacuo* with a step of 1 nm, allowing the resulting hyperspectral $Q_{bb}(\lambda)$ values to be adapted for use with any combination of visible optical wavebands pertaining to recent and currently operating ocean color multispectral sensors, or for planned (e.g. PACE (Werdell et al., 2019)) or existing hyperspectral sensors.

Before b_{bp} calculation, hyperspectral backscattering efficiencies, Q_{bb}, for each Monte Carlo run were first pre-processed by applying quality control, and band-averaging using a moving average 11-nm-wide top-hat filter, using as central wavelengths

160 the nominal bands of the following ocean color sensors: Sea-viewing Wide Field-of-view Sensor (SeaWiFS), Moderate Reso-lution Imaging Spectroradiometer (MODIS) *Aqua*, Medium Resolution Imaging Spectrometer (MERIS) and Ocean and Land

Colour Instrument (OLCI), Visible and Infrared Imager/Radiometer Suite (VIIRS) on the Suomi National Polar-orbiting Partnership (S-NPP), plus 440 and 550 nm, resulting in 19 unique bands for band-averaged backscattering efficiencies, denoted here as $\overline{Q_{bb}(\lambda)}$. The band-averaged spectral particulate backscattering coefficient, $b_{bp}(\overline{\lambda})$ was then calculated from the $\overline{Q_{bb}(\lambda)}$

165 values and the input PSD as follows (e.g. van de Hulst (1981); Kostadinov et al. (2009)):

$$b_{bp}(\overline{\lambda}) = \int_{D_{\min}}^{D_{\max}} \frac{\pi}{4} D^2 \overline{Q_{bb}}(D, \overline{\lambda}, m) N_0 \left(\frac{D}{D_0} \right)^{-\xi} dD \tag{3}$$

where m is the complex index of refraction (specified separately for coat and core in the case of phytoplankton). Equation 3 is applied separately to the phytoplankton and NAP modeled Q_{bb} values, and for each of the 3000 Monte Carlo runs. Band-averaged total $b_{bp}(\overline{\lambda})$ spectra are then calculated as the linear sum of phytoplankton and NAP backscattering. ~~Other IOPs~~

170 ~~can be calculated using Eq. 3 by substituting the backscattering efficiency with the corresponding efficiency for the IOP, e.g.~~ ~~absorption.~~

2.3 PSD retrieval via Spectral Angle Mapping

2.3.1 End-member construction

Band-averaged total $b_{bp}(\overline{\lambda})$ spectra were used to construct the backscattering *end-members*, $E(\overline{\lambda})$, corresponding to ~~a specific~~

175 ~~value~~ specific input values of the PSD slope ξ. First, individual total b_{bp} spectra from each Monte Carlo run (N= 3000) were normalized by the value at 555 nm. The median of all normalized spectra at each waveband was used as the end-member for each PSD slope, from $\xi=2.5$ to $\xi = 6$ in steps of 0.05 (see Table 1). This approach allows the isolation of b_{bp} spectral shape (dependent on ξ), and spectral magnitude (dependent on N_0) (Eq. 3). Using the hyperspectral underlying Q_{bb} values, end-members can be constructed for any desired set of wavelengths.

180 #### 2.3.2 PSD parameter retrieval and operational application to OC-CCI ocean color data

The PSD parameters ξ and N_0 are retrieved using the backscattering end-members, $E(\overline{\lambda})$, via the spectral angle mapping (SAM) technique (e.g. Dennison et al. (2004)). Briefly, the end-members and satellite-observed b_{bp} spectra are treated as n-dimensional vectors where n is the number of bands. The spectral angle between a given end-member and the observed spectrum is then calculated using the vector dot product as:

185 $$\Theta = cos^{-1} \left(\frac{\boldsymbol{b_{bp}(\overline{\lambda})} \cdot \boldsymbol{E(\overline{\lambda})}}{||\boldsymbol{b_{bp}(\overline{\lambda})}|| \, ||\boldsymbol{E(\overline{\lambda})}||} \right) \tag{4}$$

Thus, spectral angle is an index of spectral shape similarity between two spectra, with more similar spectral shapes resulting in lower spectral angles. Equation 4 was used to calculate the spectral angle Θ between each of the 71 end-members, $E(\overline{\lambda})$, and the input observed $b_{bp(\overline{\lambda})}$ spectrum. The value of ξ corresponding to the smallest spectral angle is then assigned as the

retrieved PSD slope. Three wavebands were used, namely 490, 510 and 550 nm. For operational application to OC-CCI v5.0

190 (Sathyendranath et al., 2021) data (which does not have the 550 nm band), band-shifting was applied to the input $R_{rs}(560)$ to estimate the corresponding $R_{rs}(550)$, which is used in the Loisel and Stramski (2000) IOP inversion. The band-shifting was constructed using the band ratios between the respective original and target bands from a hyperspectral run of the Morel and Maritorena (2001) (MM01) model. No other bands were shifted.

The N_0 parameter is subsequently retrieved as the ratio of 1) the satellite observed value of $b_{bp}(443)$ and 2) the median value

195 of the quantity $b_{bp}(443)/N_0$ corresponding to the end-member class of the retrieved ξ and all statistically similar classes (see Supplement Sec. S1) across all Monte Carlo simulations.

2.4 Derived products: Size-partitioned phytoplankton carbon, PSCs, POC and Chlorophyll

Once the PSD parameters are known, they can be used to compute derived products (Kostadinov et al., 2010, 2016a; Roy

et al., 2017)). Phytoplankton carbon in any size class spanning from cell diameter D_{min} to cell diameter D_{max} (in m) can be

200 estimated as:

$$\text{phyto C} = \int_{D_{\min_\phi}}^{D_{\max_\phi}} 10^{-9} a \left(10^{18} \frac{\pi}{6} D^3 \right)^b N_{0\phi} \left(\frac{D}{D_0} \right)^{-\xi} dD \qquad (5)$$

where $N_{0\phi} = \frac{1}{3} N_0$, and N_0 (m^{-4}) for the total PSD is the satellite-retrieved parameter from total particulate backscattering; the other PSD parameters are as in Eq. 1. Equation 5 was used to compute size-partitioned phyto C in three size classes - picophytoplankton (0.2 to 2 μm in diameter), nanophytoplankton (2 to 20 μm in diameter) and microphytoplankton (20 to 50

205 μm in diameter), as well as total phyto C as the sum of the three classes. Carbon-based PSCs are defined as the fractional contribution of each of the three size classes to total phyto C (Kostadinov et al., 2016a). Given the first-order correspondence between PSCs and PFTs (e.g. Quéré et al. (2005)), these PSCs can also be interpreted as PFTs. The allometric coefficients of Roy et al. (2017) are used here, namely $a = 0.54$ and $b = 0.85$; when cell volume V is expressed in μm^3, cellular carbon is computed in pg C per cell using these coefficients (Eq. 5, see also Menden-Deuer and Lessard (2000)). Phyto C in Eq. 5

210 is given in mg m^{-3}; the conversion factors in Eq. 5 are used to convert from m^3 to μm^3, and from pg to mg C (Kostadinov et al. (2016a); Roy et al. (2017)). The factor of $\frac{1}{3}$ is an assumption of the model (Tables 1 and 2). Thus, an estimate of POC (computed using the same size limits as total phyto C) was calculated as $3 \times$ phyto C.

Chlorophyll concentration was estimated from the PSD retrievals and the input intracellular chlorophyll concentration, Chl_i (Table 1; Roy et al. (2017)) as follows:

$$215 \quad \text{Chl} = \int_{D_{\min_\phi}}^{D_{\max_\phi}} \frac{\pi}{6} D^3 Chl_i N_{0\phi} \left(\frac{D}{D_0} \right)^{-\xi} dD \qquad (6)$$

Here, Chl_i, D, D_0 and $N_{0\phi}$ all have to be expressed in consistent units so that Chl is obtained in $\mathrm{mg\,m^{-3}}$. Here we use the median Chl_i across all Monte Carlo simulations to produce a single Chl estimate.

2.5 Validation and Comparison

A data set of near-surface *in-situ* PSD measurements was compiled for validation of the PSD parameter products, ξ and
220   N_0 (Eq. 1). The data set consists of ~~mostly Coulter counter measurements, some LISST~~Coulter counter and Laser In-Situ Scattering and Transmissometry (LISST) measurements, and a small set of PSDs derived from multiple instruments and modeling. Specifically, the compilation consists of the following data sets: 1) a compilation of several data sets of Coulter counter measurements, as used in the KSM09 algorithm validation in Kostadinov et al. (2009), 2) LISST-100X (Sequoia Scientific©) measurements from the Plumes and Blooms Project (e.g. Toole and Siegel (2001); Kostadinov et al. (2007)) in the Santa Bar-
225   bara Channel, as used in Kostadinov et al. (2012), 3) Coulter counter measurements from the Atlantic Meridional Transect cruise #26 (AMT26) (Organelli and Dall'Olmo, 2018), as compiled and used in Organelli et al. (2018, 2020); 4) In-line LISST 100-X measurements from the following cruises: North Atlantic Aerosols and Marine Ecosystems Study (NAAMES) 3 and 4 (https://doi.org/10.5067/SeaBASS/NAAMES/DATA001; https://science.larc.nasa.gov/NAAMES/), EXport Processes in the Ocean from Remote Sensing (EXPORTS) North Pacific (NP), and EXPORTS North Atlantic (NA) (https://doi.org/10.5067/
230   SeaBASS/EXPORTS/DATA001; https://oceanexports.org/); and 5) PSDs obtained using a VSF-inversion technique (Zhang et al., 2011, 2012) from the volume scattering functions (VSFs) measured during the NASA EXPORTS campaign (Siegel et al., 2016) in the North Pacific in 2018 (Siegel et al., 2021).

The compiled PSD data set was used to fit for the PSD parameters of Eq. 1 using the 2 to 20 µm diameter range. One data point was removed from the 2018 EXPORTS PSD data due to a poor fit to a power-law PSD. These *in-situ* estimates were
235   matched to satellite OC-CCI v5.0 (Sathyendranath et al., 2019, 2021) satellite R_{rs} using the same matching methods described below for POC and pico-phytoplankton carbon data. Matched reflectances were used as input to the novel PSD algorithm presented here. The *in-situ* and satellite PSD parameters were then compared using a type II linear regression and several additional algorithm performance metrics (e.g. Seegers et al. (2018)), details of which are given in the Fig. 8 caption.

A large compilation of *in-situ* POC data was collected from various public databases and private contributors and was used
240   here to perform match-ups with satellite OC-CCI v5.0 data. In addition to the POC data (1997-2012) used in Evers-King et al. (2017) for algorithm validation (N = 3891), this study also incorporated recent *in-situ* POC data (2013-2020) from the SeaWiFS Bio-optical Archive and Storage System archive (https://seabass.gsfc.nasa.gov/). The daily, 4 km, sinusoidal projection OC-CCI v5.0 data (1997-2020) (Sathyendranath et al., 2019, 2021) were used to extract the closest central satellite pixels to the *in-situ* data points. If the central satellite match-up pixels was valid, the surrounding eight pixels (a 3 x 3 pixel box) were also
245   extracted to estimate the mean, median, and standard deviation of all OC-CCI variables. The match-up data points were then averaged with respect to depth (0 to 10 m), location, and date. Moreover, a number of uncertain match-up data points ~~(e.g. with less than 4 valid pixels out of 9) were removed~~were removed, as described below. A total number of 6041 match-up data points were obtained and used for analysis. Here, the median satellite $R_{rs}(\lambda)$ matched-up ~~variables~~spectra were used to compute the

satellite-retrieved POC data using the PSD-based algorithm. ~~Duplicate in-situ match-ups (in the sense of points receiving the same satellite match-up) were treated as separate match-up points.~~

The *in-situ* pico-phytoplankton carbon data set compiled and used for algorithm inter-comparison as part of the ESA POCO project (Martínez-Vicente et al., 2017) was used here to generate match-ups with satellite OC-CCI v5.0 R_{rs} data for further validation. Match-ups were generated in the same way as described above for POC.

All *in-situ* data described above were excluded from the validation if any of the following conditions were met: 1) average bathymetric depth from an ≈ 9 km buffer around the *in-situ* sample location was less than or equal to 200 m, or any grid cell elevations in that buffer were 0 m or higher, using a downsampled, 4 km version of the NOAA ETOPO1 data set (https://www.ngdc.noaa.gov/mgg/global/); 2) the *in-situ* sample depth was 15 m or greater, or 3) there were ~~four~~ three or fewer satellite pixels available to use in the match-up, as detailed above.

All duplicate in-situ match-ups (in the sense of multiple *in-situ* data points that are close in space and time and receiving the same satellite match-up) were combined into a single match-up point as follows: for the PSD, the medians of the PSD measurements from the NAAMES and EXPORTS cruised in each LISST size bin for such duplicates were used for the calculation of *in-situ* PSD parameters (a large number of duplicates since the data is in-line); for the rest of the PSD data, the fit PSD parameters themselves were averaged (a small number of duplicates). For the POC (large number of duplicates) and pico-phytoplankton carbon data (small number of duplicates), the averages of the duplicate *in-situ* were used.

In addition to validation against *in-situ* measurements of the PSD, POC and pico-phytoplankton carbon, satellite chlorophyll-a (Chl) retrievals (using the standard algorithm of OC-CCI v5.0 at the match-up points) were compared with Chl estimated using the ~~EAP-based formulation of the PSD algorithm developed here and the retrieved PSD~~ PSD retrieval (Eq. 6). Finally, global algorithm retrievals of total phyto C for May 2015 (using OC-CCI v5.0 data as input) were also compared with two alternative methods of retrieving phyto C: 1) the Roy et al. (2017) algorithm, and 2) the Graff et al. (2012, 2015) algorithm, as implemented by NASA's Ocean Biology processing Group (OBPG). Modeling and processing of results presented here is done using the sinusoidal projection images; maps presented here are given in equidistant cylindrical projection (i.e. un-projected latitude/longitude).

3 Results and Discussion

3.1 Forward and Inverse Modeling

The first step in the algorithm development is the generation of 3000 Monte Carlo realizations of backscattering efficiencies as a function of particle diameter and wavelength, $Q_{bb}(D, \lambda)$. The important differences between backscattering efficiencies of homogeneous and coated particles is discussed in Supplement Sec. S2~~and illustrated in Supplement Fig. S2~~. Here, we continue the discussion with the resulting integrated backscattering spectra (Eq. 3. Hyperspectral $b_{bp}(\lambda)$ spectra modeled using a single forward optical model run are shown in Fig. 1. The computations use the median values of inputs ~~that are~~ varied in the Monte Carlo simulations (Tables 1 and 2). These normalized spectra illustrate the strong spectral shape dependence on the PSD slope ξ. Phytoplankton b_{bp} spectral shapes are complex, with various peaks and troughs near the absorption peaks of chlorophyll, but

are more linear in the 490 to 550 nm range, which is the one used for the multi-spectral operational PSD algorithm. Regardless, the SAM methodology of retrieval here allows for any spectral shape and does not impose a power-law fit to the shape of b_{bp}, as is done in KSM09 (Kostadinov et al. (2009)) (see also Loisel et al. (2006)). NAP backscattering exhibits smooth shapes due to the smooth shape of their absorption (Fig. 1B). Fundamentally, it is evident from Figs. 1A and 1B that the higher the PSD slope ξ, the steeper b_{bp} spectral shape becomes, with higher values in the blue, since smaller particles dominate the signal. This dependence is at the root of the principle of operation of the PSD algorithm. For completeness, corresponding absorption spectra are illustrated in Supplement Fig. S3.
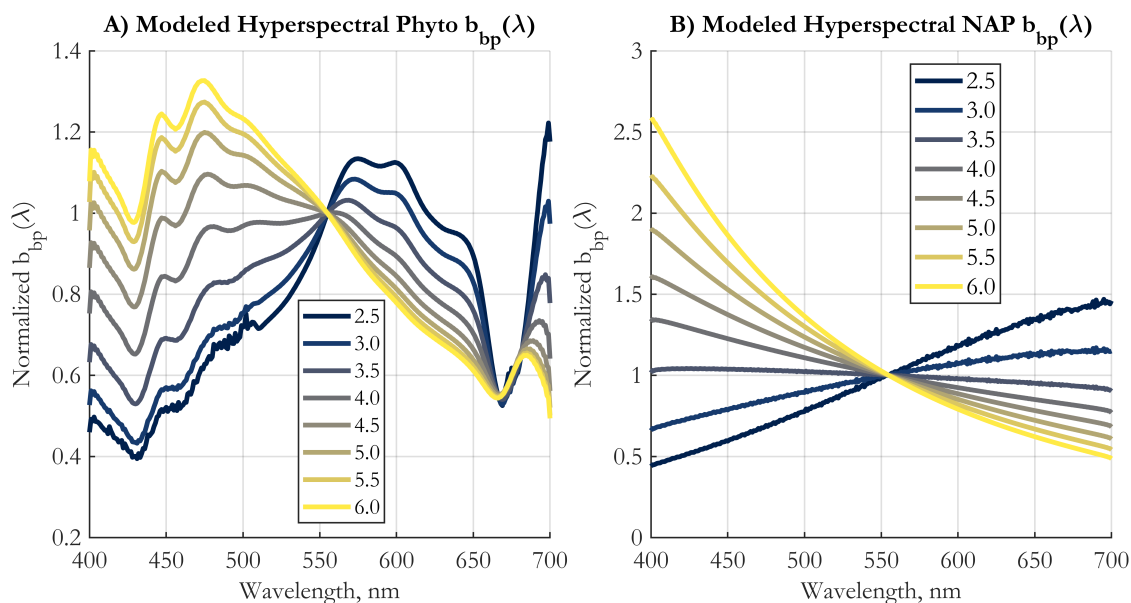
Figure 1. Modeled hyperspectral backscattering coefficient by (A) phytoplankton, using EAP-based coated spheres Mie scattering computations, and (B) NAP, modeled as homogeneous spheres, as a function of the input power-law PSD slope (color-coded solid lines, as in legend). All spectra are shown normalized to the respective values at 555 nm. See Sec. 2 for more details.

The 71 end-members (EMs) created for operational application to existing major satellite ocean color missions and corresponding to PSD slope values between 2.5 and 6.0 with a step of 0.05 are displayed in Fig. 2A. They represent the modeled $b_{bp}(\overline{\lambda})$ spectra against which satellite-measured b_{bp} spectra are compared using the SAM method (Eq. 4). The spectral shape dependence on ξ demonstrates the theoretical ability to retrieve this parameter from space.

An important question in bio-optical oceanography is determining the sources of backscattering in the ocean and their relative contributions. This is still not a resolved issue (Stramski et al., 2004), though progress has been made (e.g. Organelli et al. (2018); Koestner et al. (2020); Zhang et al. (2020)). This issue is of central importance to the PSD model, as it assigns varying fractions of the b_{bp} signal to phytoplankton vs. NAP, under certain assumptions (Tables 1 and 2). Since in the 2-component PSD model presented here phytoplankton and NAP b_{bp} are modeled separately, the fraction of b_{bp} due to phytoplankton vs. NAP can be calculated. For a given PSD slope ξ and wavelength, the assumptions of the model dictate fixed fractional contributions
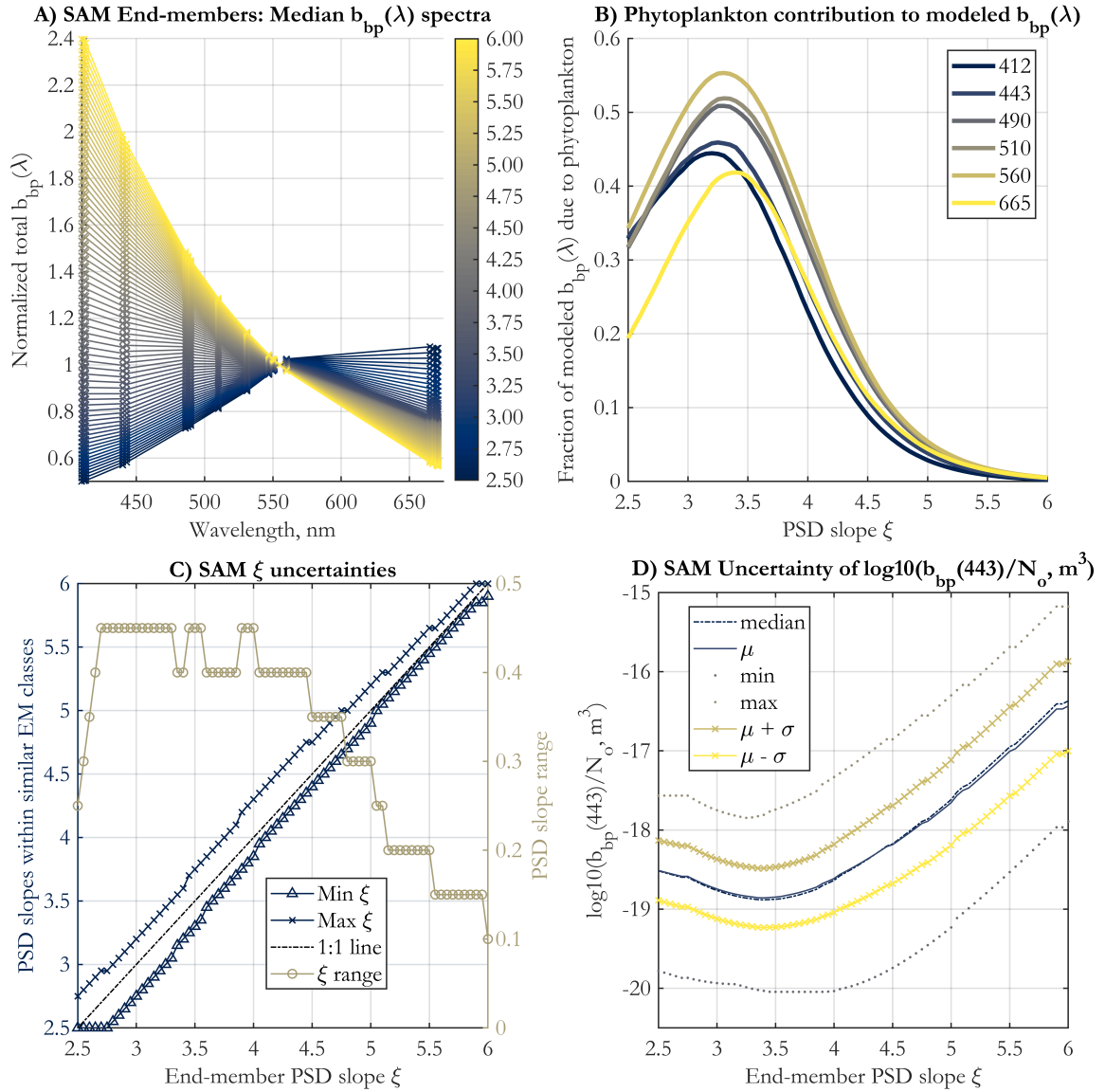
Figure 2. (A) Normalized spectral shapes of the b_{bp} end-members (EMs)developed for spectral angle mapping (SAM), shown at the 19 unique wavelengths used for band-averaging (See Sec. 2.2), and for PSD slopes as in the color legend. (B) The fraction of $b_{bp}(\lambda)$ due to phytoplankton as a function of the PSD slope ξ. The wavelengths shown are indicated in the legend (nm). The means across all 3000 Monte Carlo simulations are shown. (C) Uncertainties in the PSD slope ξ retrieval using the SAM method, for each ~~end-member~~ (EM). Shown are the minimum and maximum value of the PSD slope for all end-member classes that are statistically similar to the given EM, according to the Kruskal-Wallis ANOVA (Supplement Sec. S1) (left y-axis), and the resulting range of PSD slopes (right y-axis) falling within these asymmetric uncertainty bounds. (D) Statistics of the parameter $log10(b_{bp}(443)/N_0)$ for each EM, calculated for all 3000 Monte Carlo simulations and across all neighboring EM classes determined to be statistically similar to the given EM. μ in the legend stands for the mean, and σ - the standard deviation. The standard deviation of this parameter is used to estimate uncertainties in the N_0 retrieval.

by NAP and phytoplankton to total b_{bp}, which are given in Fig. 2B. There is variability by wavelength, but the first-order variability is driven by the PSD slope, namely at low ξ values ($\xi < 4.0$), phytoplankton contribution to b_{bp} is on the order of 30 to 50%, and it drops off to near 0% for higher slopes as ξ approaches 6.0. The curves are not monotonic, and peak phytoplankton contribution to b_{bp} occurs at $\xi \approx 3.25$.

The fractional contributions of Fig. 2B are derived from the forward theoretical modeling, and they are influenced by all model assumptions and are not validated independently. In particular, the decisions of integration diameter limits for NAP and phytoplankton, as well as on the distributions of the indices of refraction for phytoplankton and NAP will have a strong influence on these values. Since NAP are here permitted to have higher RIs than RIs typical of organic detritus only, if NAP were strongly dominated by or composed only of organic particles, then NAP contribution to b_{bp} would be overestimated here. Of course these RIs are likely to be spatially and temporally variable, and the algorithm can be further improved by investigating and implementing such variability. Bellacicco et al. (2018) estimated global absolute b_{bp} due to NAP and its fractional contribution to total b_{bp} using analysis of correlations with Chl. Qualitatively and to first order, their global pattern of percent b_{bp} due to NAP agrees with the model results reported here, i.e. low relative NAP contributions in high latitudes and eutrophic areas, and higher relative contributions in more oligotrophic areas such as the fringes of the subtropical gyres (they exclude the gyres from their analysis) (cf. their Fig. 2C and Fig. 2B here). Note that the Bellacicco et al. (2018) estimate pertains only to NAP non-covarying with Chl, making comparison harder. Further investigation is warranted to more rigorously compare their product to the values implicit in the PSD algorithm described here. Apart from analyzing the relative contribution of phytoplankton vs. NAP to total b_{bp}, it is of interest to investigate the relative contributions of various size ranges to the modeled backscattering coefficient. This is illustrated in Supplement Fig. S4 and further discussed in Supplement Sec. S3.

The uncertainty in PSD slope ξ retrieval as a function of ξ is illustrated in Fig. 2C. These estimates are not symmetric about the ξ value and are derived via Kruskal-Wallis analysis of variance to determine class similarity (Supplement Sec. S1). As in KSM09, the general tendency is for the range of uncertainty in ξ to increase for lower PSD slopes, but it is always less than 0.5. The uncertainty in the $b_{bp}(443)/N_0$ ratio used to retrieve the N_0 parameter is shown in Fig. 2D in log10 space. Mean and median values are similar, and the uncertainty about them does not vary much with PSD slope, also similarly to KSM09. ~~Importantly, the~~ The uncertainty in Fig. 2D at each ξ value includes all statistically similar classes of EMs.

3.2 Operational Application of the PSD/Phyto C Algorithm to OC-CCI v5.0 Merged Satellite Data

3.2.1 PSD Parameters

The operational PSD algorithm presented here was applied to the monthly 4-km OC-CCI v5.0 $R_{rs}(\lambda)$ data set (Sathyendranath et al. (2019, 2021)). Both PSD parameters (ξ and N_0, Eq. 1) and derived products were generated (Sec. 2.3 and Sec. 2.4). These data and their monthly and overall climatologies (and associated uncertainties) are made publicly available (see 4). Here, we use May 2015 data to illustrate and discuss the new algorithm.

The PSD map (Fig. 3A) reveals a global spatial pattern consistent with expectations and with KSM09, namely the subtropical oligotrophic gyres are characterized by high PSD slopes ~~, i.e.~~ (relatively high numerical dominance of small particles),

whereas more eutrophic areas such as coastal areas, Equatorial upwelling zones, and high latitudes exhibit lower slopes ~~, i.e.~~ (increasing relative abundance of larger particles). This is consistent with oligotrophic ocean ecosystems being dominated by picophytoplankton, whereas microphytoplankton contribute significantly to the phytoplankton assemblage in eutrophic areas

335 and during blooms (e.g. Kostadinov et al. (2009, 2010) and refs. therein). PSD slope values retrieved by the SAM-based algorithm span the full modeled range of $2.5 \leq \xi \leq 6.0$. This is in contrast to KSM09, where values below 3.0 were not retrieved. The N_0 PSD parameter (Eq. 1) is, as expected, higher in coastal, high latitude and eutrophic areas (indicating higher particle loads), and lower in the oligotrophic subtropical gyres (Fig. 3B). N_0 varies over a few orders of magnitude ~~, and it is generally the first order control on absolute particle loads in seawater~~. Note N_0's units of m^{-4} (Eq. 1) and that care should be taken when

340 comparing Eq. 1 and N_0 to other formulations of the PSD, e.g. the k parameter in Roy et al. (2017), as these are related, but not equivalent (see also Vidondo et al. (1997)).
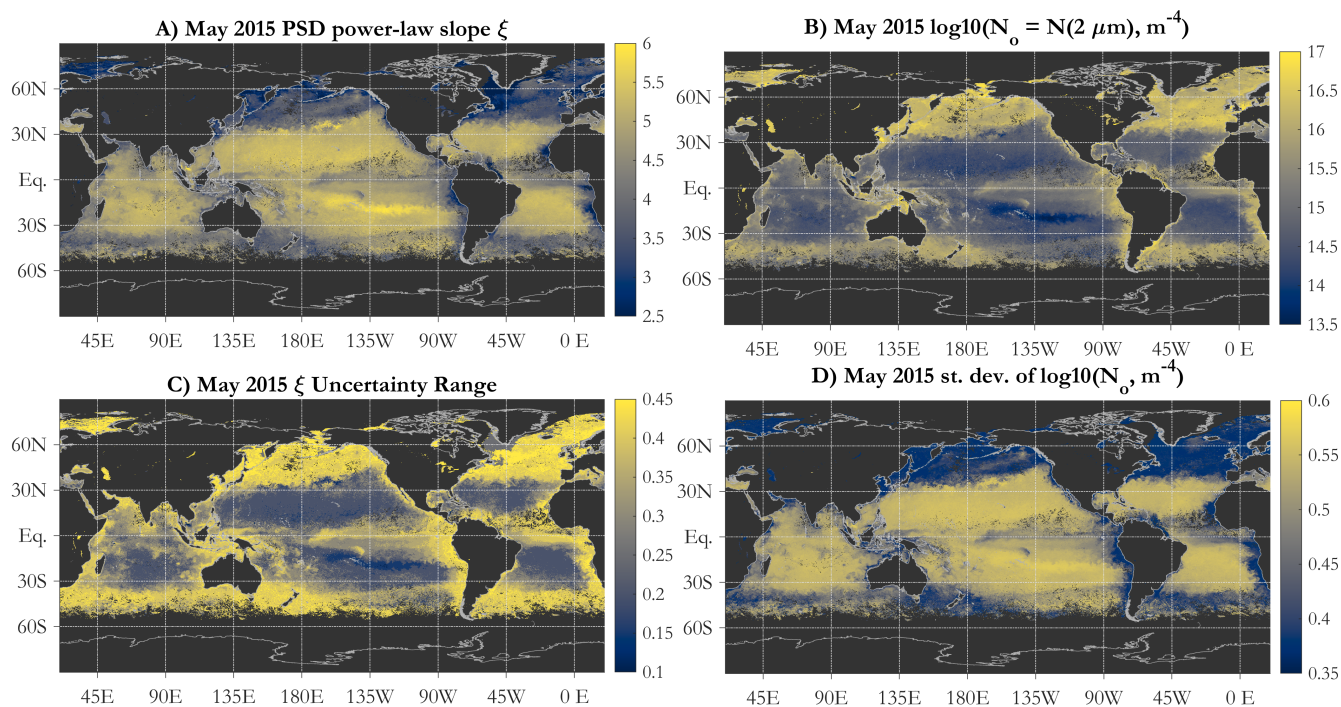
Figure 3. Example operational retrievals of the PSD parameters (Eq. 1) and their uncertainties, using monthly OC-CCI v5.0 R_{rs} data for May 2015: (A) PSD slope ξ (A); (B) N_0 parameter (in m^{-4} in log10 space); (C) uncertainty range for ξ, and (D) standard deviation of log10 of N_0.

Algorithm uncertainties are provided on a per-pixel basis. The uncertainty range estimates for ξ (Fig. 3C) (not necessarily symmetric about the ξ value) indicate that the gyres are characterized by lower uncertainties than the more eutrophic areas, as can be expected from Fig. 2C. These are partial uncertainty estimates, including those quantifiable and internal to the modeling,

345 i.e. due to Mie parameter choices. Additional uncertainties inherent in the input OC-CCI R_{rs} values and those due to the IOP

inversion algorithm used are not included in Fig. 3C and 3D and in subsequent propagated errors. Uncertainties of the N_0 parameter are more uniform spatially, but higher in the gyres (Fig. 3D. Note that those are given in log10 space as a standard deviation, and a relatively small absolute value of the uncertainty translates to relatively large uncertainties in absolute particle concentrations.

350 ### 3.2.2 Phytoplankton Carbon and Carbon-based PSCs; POC and Chlorophyll from the PSD

Global patterns of total phytoplankton carbon (phyto C) retrieved via the PSD and allometric relationships (Fig. 4A) exhibit the expected lower values in the oligotrophic gyres and higher values elsewhere. Similarly to the results of ~~the Kostadinov et al. (2016a) algorithm~~Kostadinov et al. (2016a), values range over approximately 3 orders of magnitude, which is a higher range than re-trievals based on other methods, namely direct empirical algorithm POC retrieval (Stramski et al., 2008) or the Behrenfeld 355 et al. (2005) method of scaling backscattering, and it is also higher than the range in CMIP5 model ensembles (cf. Fig. 1 in Kostadinov et al. (2016a)). This putative underestimation in the gyres and overestimation in eutrophic areas suggests the need for algorithm tuning, which is discussed in Sec. 3.3 along with implications of validation results. Global validation of phyto C retrievals with analytical phyto C measurements is planned, but is currently challenging as phytoplankton-specific carbon data are relatively novel (Graff et al., 2012, 2015) and still scarce. Here, an initial validation effort is undertaken using several other 360 variables, see Sec. 3.3.
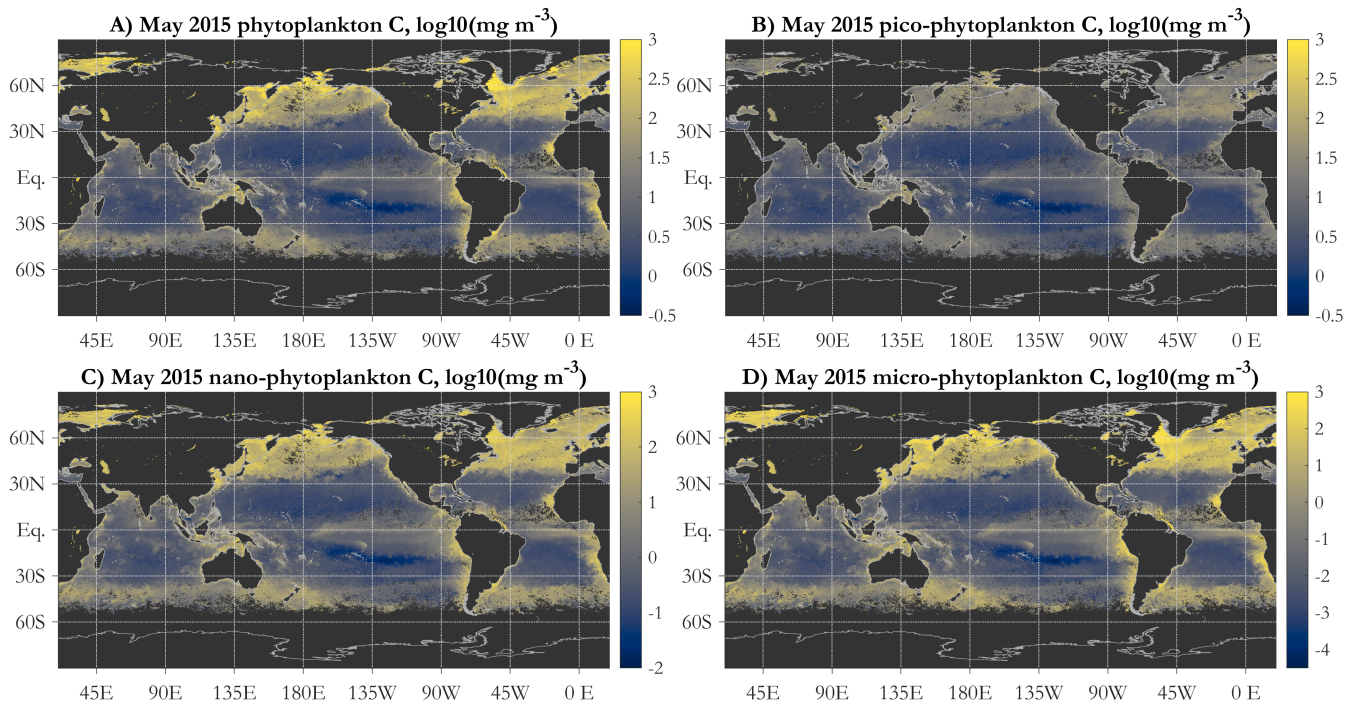
Figure 4. Example operational PSD-based retrievals of total size-partitioned phytoplankton carbon, using monthly OC-CCI v5.0 R_{rs} data for May 2015: total phytoplankton carbon (A), pico-phytoplankton carbon (B), nano-phytoplankton carbon (C), and micro-phytoplankton carbon (D). Units are $\mathrm{mg\,m^{-3}}$, mapped in log10 space. The diameter limits for the three size classes are: picophytoplankton (0.2 to 2 µm), nanophytoplankton (2 to 20 µm) and microphytoplankton (20 to 50 µm).

A key feature of the PSD-based algorithm is that phyto C can be partitioned into any number of size classes by choosing appropriate integration limits of Eq. 5. Absolute concentrations of pico-, nano-, and micro-phytoplankton are illustrated for May 2015 in Fig. 4B, C, and D, respectively. Pico-phytoplankton C is mapped on the same color scale as total phyto C (Fig. 4A), but pico- and nano-phytoplankton C maps have differing scales, illustrating that while pico-phytoplankton C varies over ≈3

365   orders of magnitude spatially globally, nano-phytoplankton C varies over ≈4-5 orders of magnitude, and micro-phytoplankton — over ≈7 orders of magnitude spatially (see also Kostadinov et al. (2010, 2016a). Note that empirical tuning will affect these ranges of variability, see Sect. 3.3. Fractional contributions of each of the three PSCs used here to total phyto C are illustrated in Fig. 5. Pico-phytoplankton dominate much of the open-ocean, lower latitude oligotrophic areas, contributing nearly 100% of the carbon biomass there (Fig. 5A), nano-phytoplankton contribute up to ≈50% of biomass in the higher latitude and

370   more eutrophic areas, and micro-phytoplankton contribute significantly only in the most eutrophic areas, e.g. during the North Atlantic bloom at ≈45-50° N latitude (May 2015 is shown). As previously noted (Kostadinov et al., 2010, 2016a), this general pattern is consistent with current understanding of ocean ecosystems.
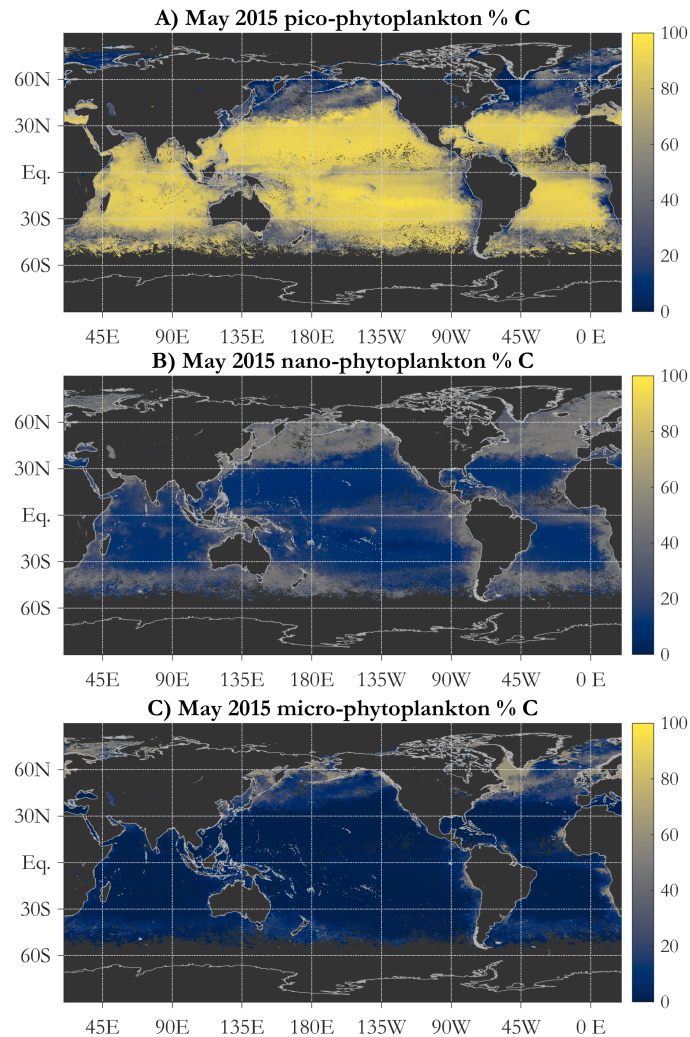
Figure 5. Example operational retrieval of the percent contribution of each phytoplankton size class (PSC) to total phytoplankton carbon, determined via the PSD (Sec. 2.4). Retrievals are using monthly OC-CCI v5.0 R_{rs} data for May 2015. The PSCs are: pico-phytoplankton (A), nano-phytoplankton carbon (B), and micro-phytoplankton carbon (C).

The fractional carbon-based PSCs (Fig. 5) are ratios of two integrals of Eq. 5, thus they are analytical functions of the PSD slope ξ and the b ~~, the~~ allometric coefficient (~~and~~ as well as the limits of integration used for each class and total phyto C). ~~The~~ ~~N_0 parameter and the a allometric coefficient cancel.~~ These functions are plotted in Fig. 6, together with the satellite-observed ξ histogram for May 2015, illustrating which the most common values for the PSCs in the ocean are. Area-wise, the ocean is dominated by oligotrophic areas with high pico-phytoplankton contributions to C biomass.
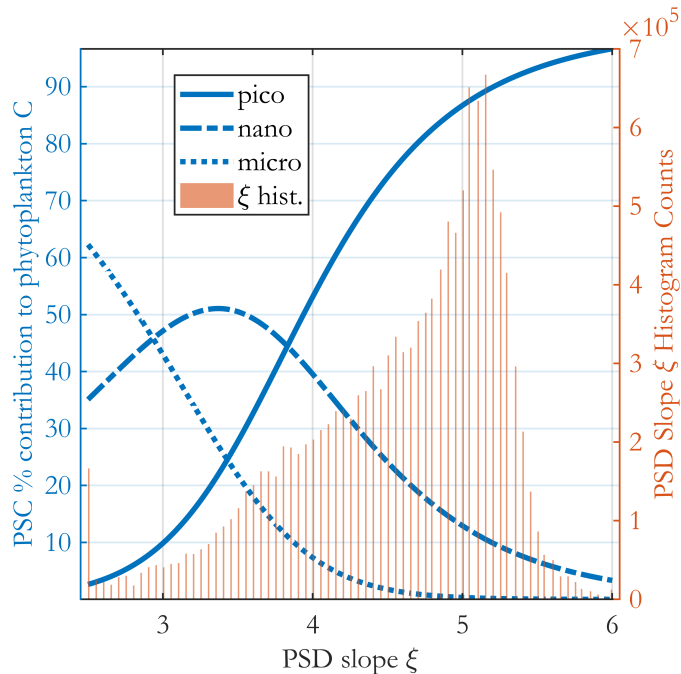
Figure 6. Percent contribution of each PSC to total phytoplankton carbon (blue curves as in legend, left y-axis), as a function of the PSD slope ξ. A histogram of the PSD slope from the (sinusoidal projection) OC-CCI v5.0-based image for May 2015 is shown in the background in ~~as~~ red ~~bars~~ (right y-axis). The three PSC curves are analytically derived from the model, and no satellite data is used in producing them.

As an illustration of uncertainty propagation to derived products, the propagated uncertainty to total phyto C (Fig. 7A) and fractional pico-phytoplankton C biomass (Fig. 7B) are shown. Comparison of Fig. 4A with Fig. 7A indicates that absolute total phyto C uncertainties are of the same order of magnitude as the values themselves. ~~As noted earlier, this~~ This is a partial uncertainty estimation due to the assumed distributions of the Mie inputs (Tables 1 and 2), and due to the allometric coefficients. The Mie inputs are varied over wide ranges to accommodate various environments in the global ocean, with the goal of having a single first-principles-based operational algorithm applicable to first order globally. This increases the uncertainty estimates. The uncertainty for the fractional PSC products depends only on the uncertainties in ξ and b, thus they exhibit much lower internal algorithm uncertainty compared with absolute values. For pico-phytoplankton, they are $< \approx 2\%$ for the oligotrophic gyres, and do not exceed $\approx 7\%$ globally. ~~As stated above, the N_0 parameter and a (the allometric coefficient) cancel when fractional PSCs are calculated, thus they exhibit much lower internal algorithm uncertainty compared with absolute values.~~ This suggests that the fractional PSCs are more reliable products than the absolute values, and they can also be used with other products to partition them - e.g. total phytoplankton carbon estimated using the alternative methods shown in Fig. 9 (namely Graff et al. (2015) and Roy et al. (2017)), or the Behrenfeld et al. (2005) or Sathyendranath et al. (2020) methods; POC products (e.g. Stramski et al. (2008)) can be partitioned this way as well. ~~Figs. 7A and 7B illustrate some propagated~~

~~uncertainties.~~ Per-pixel uncertainties are estimated for all products and composite imagery ~~as well~~ (climatologies) as well, and are provided with the OC-CCI-based data set associated with this manuscript (Sec. 4).
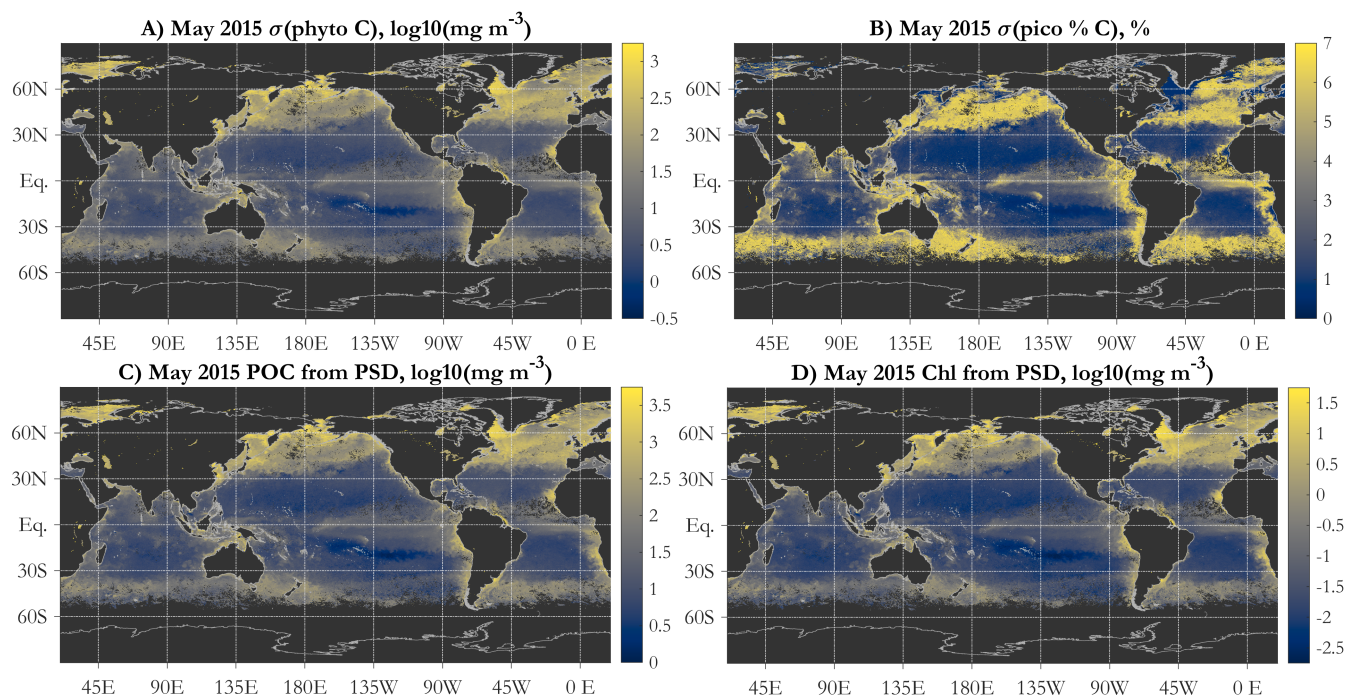
Figure 7. Propagated uncertainty of (A) total phytoplankton carbon given as one standard deviation (in $\mathrm{mg\,m^{-3}}$), mapped in log10 space, and (B) fractional contribution of pico-phytoplankton to total phytoplankton carbon, given as one standard deviation in percent. (C) POC derived using the PSD retrievals, (in $\mathrm{mg\,m^{-3}}$), mapped in log10 space; and, (D) Chlorophyll concentration (Chl) derived using the PSD retrievals, (in $\mathrm{mg\,m^{-3}}$), mapped in log10 space. Monthly OC-CCI v5.0-based data for May 2015 is shown in all panels.

The formulation of the PSD algorithm allows for both POC and Chl (Eq. 6) to be estimated from the retrieved PSD. Due
395   to the assumptions used, POC is phyto C multiplied by three (Fig. 7C). This is strictly true only if the POC estimate uses the same limits of integration as phyto C, which is an approximation to the usual POC operational definition (e.g. see discussion of POC-PSD closure analysis in Kostadinov et al. (2016a)). POC thus is estimated to first order, treating the retrieved NAP as being composed of POC only, and applying the same allometric relationships to it as phyto C, in spite of the fact that the assumed RI distribution of the NAP is broader (Table 2). These are simplifying assumptions of the 2-component model; a
400   more accurate POC representation can be achieved if organic and inorganic NAP are modeled as separate particle populations (e.g. Duforêt-Gaurier et al. (2018)). This is a planned development of the model in the future; the goal here is to build an operational PSD/phyto C algorithm (based on first principles, as mechanistic as feasible) for use with multi-spectral satellite data of limited degrees of freedom. Hyperspectral sensors such as PACE (Werdell et al., 2019) should allow for some more degrees of freedom and thus for more independent particle components and their PSDs to be modeled separately. However, note
405   that even hyperspectral data has limits on its degrees of freedom that are expected to be much fewer than the number of sensor

bands (Lee et al., 2007; Cael et al., 2020). An important benefit of POC is that it is a widely observed variable, available for global validation efforts (Sec. 3.3), as is Chl. Similarly to POC, there are benefits of the PSD-derived estimate of Chl (Fig. 7D) - it can be used as additional verification/validation of model retrievals, and/or PSD-retrieved Chl can be used as a parameter to optimize for in algorithm tuning, as discussed shortly (Sec. 3.3). ~~Like POC, many global *in-situ* and satellite observations of~~

410 ~~Chl are available for such efforts.~~ Next, we discuss validation/verification and tuning efforts in which both PSD-derived POC and PSD-derived Chl are used.

3.3 Algorithm Validation, Comparisons and Empirical Tuning for the N_0 PSD Parameter and Absolute Concentrations

In an initial validation effort, the novel PSD/phyto C algorithm is validated/verified using several variables. It is challenging

415 to directly globally and thoroughly validate the major products of the algorithm - the PSD and size-partitioned phyto C, due to a paucity of globally-spanning *in-situ* observations which are further reduced when performing satellite match-ups. Here, we validate or verify algorithm performance against compilations of the following variables: 1) *in-situ* PSD observations (Sect 2.5); 2) *in-situ* POC observations; 3) *in-situ* pico-phytoplankton C observations; 4) concurrent satellite observations of Chl. Maps of the locations of *in-situ* observations are shown in Supplement Fig. S5. In addition, we compare phyto C retrievals to

420 several existing methods using the example May 2015 OC-CCI v5.0 image. ~~Below we discuss the results of these validation,~~ ~~verification and comparison efforts and a suggested~~ Further, based on these results, we suggest an empirical tuning of the algorithm.

Validation results for the PSD slope ξ (Fig. 8A) indicate a statistically significant but noisy relationship between retrieved and observed slopes, with a positive bias for satellite retrievals, and ~~two distinct clusters of points for which satellite values~~

425 ~~differ - centering about 3.25 vs. 4.75, respectively, but the~~ a regression slope substantially greater than unity. Most validation points are scattered in a cloud of data between 3.0 and 4.5 that does not exhibit much correlation, and there is a somewhat separate cluster of data centered about a slope of 5.25 in the satellite retrieval that has smaller corresponding *in-situ* values ~~differ less and both cluster around 3.5 to~~ of about 4.0. There is generally a clear tendency for points from more oligotrophic areas (as indicated by Chl color coding) to exhibit higher satellite values, and more eutrophic areas to exhibit much lower

430 satellite values. This tendency is weaker for the *in-situ* observations, which tend to have a narrower range, mostly between 3.0 and 4.5. ~~The same validation regression with the points classified by location, rather than Chl, is shown in Fig. 8C. Data from~~ ~~two specific locations are numerous and also likely drive the regression to a large degree - 1) the Plumes and Blooms (PnB)~~ ~~Project LISST data , which represents a coastal site, namely the Santa Barbara Channel in California, USA (SBC), and 2)~~ ~~the Equatorial Pacific (EqPac). While at SBC the~~ To first order, the satellite data ~~underestimates PSD slopes , it overestimates~~

435 ~~them at EqPac. Data from higher latitudes from various locations in the North hemisphere, from CA coastal areas other than~~ ~~PnB, and from the Southern Ocean span a wider~~ are in the same range as *in-situ* ~~range, which is captured by the satellite~~ ~~retrievals, albeit with substantial noise. Overall, the satellite retrievals capture the~~ data and the retrievals capture the *in-situ* data trend; however, there is a pattern of having a bigger range of PSD slopes in satellite data than in the *in-situ* ~~data trend to first~~ ~~order~~ match-ups, with the algorithm underestimating low values and overestimating high values.
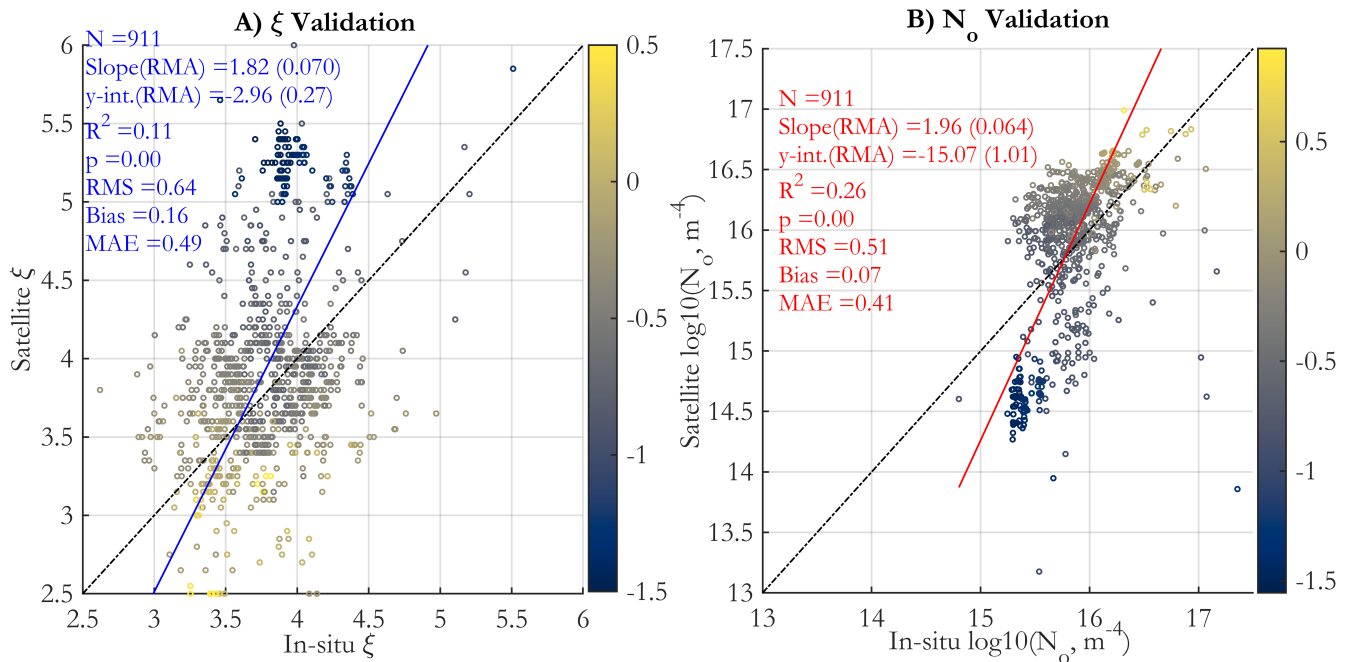
Figure 8. (A) Comparison of PSD slope derived from *in-situ* measurements with the matched-up satellite retrieval (Sec. 2.5). Points are color-coded according to the corresponding ~~matched-up~~ satellite OC-CCI v5.0 Chl (colormap in $\mathrm{mg\,m^{-3}}$ in log10 space). Type II regression is used, and regression and validation statistics are given in the figure panel. 'y-int' stands for the y-intercept, RMS - room mean square (square root of the mean of squared differences between the *in-situ* and satellite values), Bias is the mean of the satellite minus *in-situ* values, and MAE - mean absolute error (the mean of the absolute values of the differences between the *in-situ* and satellite values) (e.g. Seegers et al. (2018)). (B) Same as in panel A, for the N_0 parameter (Eq. 1) (axes in log10 space). ~~(C) The same validation regression as in panel A, but the points are color and symbol coded according to geographic area, as follows: Plumes and Blooms project (e.g. Toole and Siegel (2001); Kostadinov et al. (2007)) (PnB, green 'x'); Equatorial Pacific (EqPac, red circles); Equatorial Indian Ocean (EqIO, red '+'); Southern Ocean (SO, black '*'); California (CA) coastal area (purple squares); higher latitude Northern Hemisphere points (> 30° latitude, NH, cyan diamonds), and South Atlantic (SA, black triangles); (D) same as in panel C, but for the N_0 parameter (axes in log10 space).~~

440   Validation for the N_0 parameter (Fig. 8B) is statistically significant ~~but noisy, with a somewhat better~~ (somewhat higher R^2 ~~.~~ ~~Clustering~~ than the ξ regression) but also quite noisy. Strong clustering of the *in-situ* observations around $10^{15.5}$ - $10^{16.0}$ $\mathrm{m^{-4}}$ is observed, and the majority of these observations are ~~underestimated~~ somewhat overestimated in the satellite retrievals, which cluster around $10^{16.25}$. Notably, much lower satellite values of validation points that form a separate cluster are associated with lower Chl, and are underestimated instead - the *in-situ* values are also lower than the main cluster of point just discussed, but

445   less so. Since N_0 is the PSD scaling parameter which generally controls absolute number, volume and carbon concentrations variability to first order, this has implications for the global pattern of phytoplankton carbon retrievals (Fig. 4), namely it is consistent with underestimation in the oligotrophic gyres ~~(mostly lower Chl)~~ and overestimation in the eutrophic areas.

~~Inspection of the location-coded plot~~ Overall, both satellite and *in-situ data* exhibit increasing values of N_0 with increasing Chl concentrations, as expected — i.e. more oligotrophic waters are associated with smaller overall particle number concentrations.

Further discussion of the PSD validation by location of *in-situ* data (Fig. ~~8D) indicates that a lot of the underestimated points come from the Equatorial Pacific clustered around *in-situ* $N_0 = 10^{15.75}$; many overestimated points are from the SBC~~S5A and S5B) is provided in Supplement Sect. S4 and illustrated in Fig. S6.

This pattern of under- and overestimation in the N_0 validation drives the slope of the validation regression to be much greater than unity, and suggests an empirical tuning to absolute phytoplankton carbon ~~of the TK16 algorithm~~estimates, via a linear (in log10 space) tuning of N_0, as done in TK16 (Kostadinov et al., 2016a), who based the tuning on the validation regression. A similar approach is proposed here, but it is derived differently. Details of the tuning derivation procedure are given in Supplement Sec. S5. The following global tuning equation was obtained:

$$N_0\_tuned = 10^{0.3859 log10(N_0)+9.5531} \tag{7}$$

where N_0 is the original (un-tuned) PSD parameter. This tuning changes N_0 retrievals in a similar fashion to the TK16 tuning and is consistent with a tuning suggested by the N_0 *in-situ* validation ~~reported~~ presented here (Fig. 8B), namely, low satellite N_0 values are increased, and high N_0 values are decreased, decreasing the overall range of variability of retrieved N_0 and thus the range of the retrieved derived variables as well. This addresses the low bias in oligotrophic gyres and the high bias in eutrophic areas. The goal of the tuning is to get more realistic absolute retrievals of POC and Chl (hypothesizing that this should also lead to more realistic phyto C retrievals as well - however, see discussion below about the pico-phytoplankton C validation - Sect. 3.3.2).

The tuned N_0 parameter for May 2015 is mapped in Supplement Fig. S7A. The overall spatial pattern of higher values in more eutrophic areas is preserved, but the global range of values is reduced compared to the original value, increasing N_0 in the gyres, and decreasing it in more productive areas. The resulting multiplicative factor to be applied in linear space to phyto C, POC and Chl values is mapped in log10 space in Supplement Fig. S7B. Values in ~~red are~~ oligotrophic areas are generally greater than unity in linear space (mostly between 1 and 10), indicating that the tuning increases phyto C, POC and Chl in these areas, up to about an order of magnitude (in limited areas mostly in the South Pacific gyre), and more moderately elsewhere in the tropical and subtropical, oligotrophic oceans. The Equatorial upwelling areas and other transitional zones are not changed, and high latitude oceans exhibit correction factors mostly less than unity in linear space (mostly between 0.1 and 1), which decreases phyto C and Chl up to an order of magnitude (rare, mostly less). This tuning is not applied to figures previously discussed here.

3.3.1 Comparison of the PSD-based phytoplankton carbon retrieval with existing satellite algorithms

In this section, we compare PSD-based phyto C retrievals presented here with two existing methods for its retrieval. The May 2015 original total phyto C retrieval is compared with the tuned total phyto C and the retrievals of the absorption- and PSD-based algorithm of Roy et al. (2017) and with the Graff et al. (2015) algorithm in Supplement Fig. S8. The histograms of these four images are compared in Fig. 9. The ~~most notable feature of these comparisons is that the tuned PSD-based~~ tuned

retrievals are similar to those of Graff et al. (2015), whereas the original ~~PSD-based~~ retrievals are similar to those of Roy et al. (2017), and the latter two have exaggerated ranges globally compared to the former two. Of these algorithms, the simplest is the Graff et al. (2015), as it is a direct scaling of b_{bp}, and it is based on *in-situ* chemical analytical measurements of phyto C (Graff et al., 2012, 2015). These dichotomous inter-comparison results suggest that further algorithm inter-comparison and validation with direct *in-situ* measurements of phyto C are needed to guide future algorithm developments; however these data are relatively novel and scarce globally. Validation results using *in-situ* POC and pico-phytoplankton carbon (discussed next) exhibit a similar dichotomy.
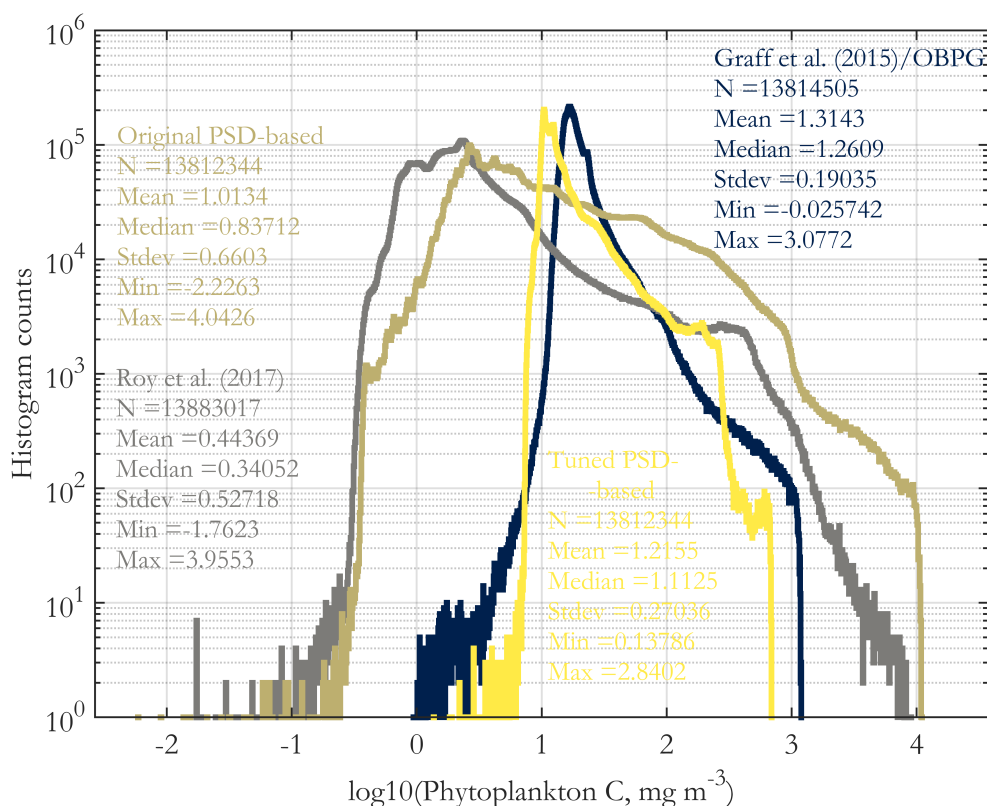
Figure 9. Histograms of the images of Supplement Fig. S8, including the original PSD-based phyto C retrieval (Fig. 4A). Histogram counts are given on a log10 scale on the y axis, and the variable (x axis) is log-transformed as well. Values less than $\approx 0.3 \, \mathrm{mg \, m^{-3}}$ are exceedingly rare for any of the retrieval variants and are shown here for completeness. All four histograms are derived from the sinusoidal projection images for May 2015, using monthly OC-CCI v5.0 data.

3.3.2 Validation using POC and pico-phytoplankton carbon *in-situ* data

PSD-based estimates of POC are validated against *in-situ* measurements for the original algorithm (Fig. 10A), and the tuned algorithm (Fig. 10C). Both regressions have satisfactory R^2 values, and also illustrate that in general higher POC values are

associated with higher Chl (colormap). Notably, the original algorithm validation has a slope of ≈ 2 and exhibits substantial underestimates at low POC, and overestimates at high POC. As intended, the tuning corrects this range exaggeration, and significantly improves the slope, intercept, bias, RMS, and MAE. The regression with the N_0 tuning applied should not be considered a truly independent validation, because the algorithm has been empirically tuned to retrieve POC well; however, the tuning was done with global POC imagery (using monthly images for 2004 and 2015) that uses the Stramski et al. (2008) empirical POC algorithm, not with these in-situ POC data directly.

In addition to the validation with *in-situ* POC, we performed a comparison of the matched satellite Chl and the corresponding PSD-based Chl estimate (Eq. 6), for the original (Fig. 10B) and the tuned algorithm (Fig. 10D). Both comparisons exhibit very high R^2 values, and similarly to POC, the original algorithm underestimated Chl at low values, and overestimated at high Chl values. The tuning successfully addresses this, leading to excellent overall comparison of the tuned algorithm, with slope near 1.0 ~~, low intercept, near nil bias, and low RMS and MAE values~~and low intercept. However, for the lowest Chl values (Chl $< 0.1 \mathrm{\,mg\,m^{-3}}$), performance deteriorates. The tuned comparison is not a fully independent validation, as the algorithm was tuned to compare well with OC-CCIv5.0 satellite retrievals (using global monthly images for 2004 and 2015). Overall, the comparison with Chl is encouraging, indicating that the model is able to reasonably reproduce (with tuning) OC-CCI v5.0 standard satellite Chl values at the match-up points.

Validation against *in-situ* pico-phytoplankton carbon is presented in Fig. 11A (with no N_0 tuning applied), and in Fig. 11C with the tuning applied. The corresponding Chl comparisons between matched standard OC-CCIv5.0 Chl and Chl derived via the PSD model are shown in Fig. 11B ~~(with no N_0 tuning applied), and in Fig. 11Dwith the tuning applied~~and D. As with the POC match-ups (Fig. 10B and D), comparisons with Chl are better for the tuned version of the algorithm, indicating that the tuning is needed to reproduce more realistic Chl values globally. However, the tuning does not lead to any improvement in the validation results of pico-phytoplankton C (cf. Fig. 11A and C). The validation regression without tuning is statistically significant (p<0.05), albeit noisy (low $R^2 = 0.18$); satellite retrievals and *in-situ* data cover approximately the same ranges, and increasing Chl and *in-situ* pico-phytoplankton C generally correspond to increasing satellite values as well, with some tendency for under- and over-estimation as with the other variables. However, the tuned satellite retrievals have a very narrow range that does not cover the range of the *in-situ* data, and validation statistics are generally worse than those of the original validation (the regression is not significant at the p=0.05 level). These validation results are generally consistent with the results of Martínez-Vicente et al. (2017), where the tuned version of the TK16 (Kostadinov et al., 2016a) algorithm was used.

~~The number of matched up sample points in the validation regression is very different among PSD, POC and pico-phytoplankton C, and their geographic distribution is different as well. Namely, there are an order of magnitude more POC match-ups than pico-phytoplankton carbon ones, and there are even fewer PSD points. A lot of the PSD data come from the Equatorial Pacific and off of California, whereas POC samples are more global with a large number coming from the Atlantic Ocean, where a lot of the pico-phytoplankton C points are located as well, and some of the latter are also from the Mediterranean. Thus the different validation results presented here do not necessarily represent the same oceanographic conditions, e.g. the pico-phytoplankton C in-situ data has less representation of eutrophic areas and spans a smaller range of Chl than the POC validation, with very few points exceeding Chl = 1.0 (cf. Fig. 10B and 11B). Furthermore, size is not the only distinguishing characteristic of the~~
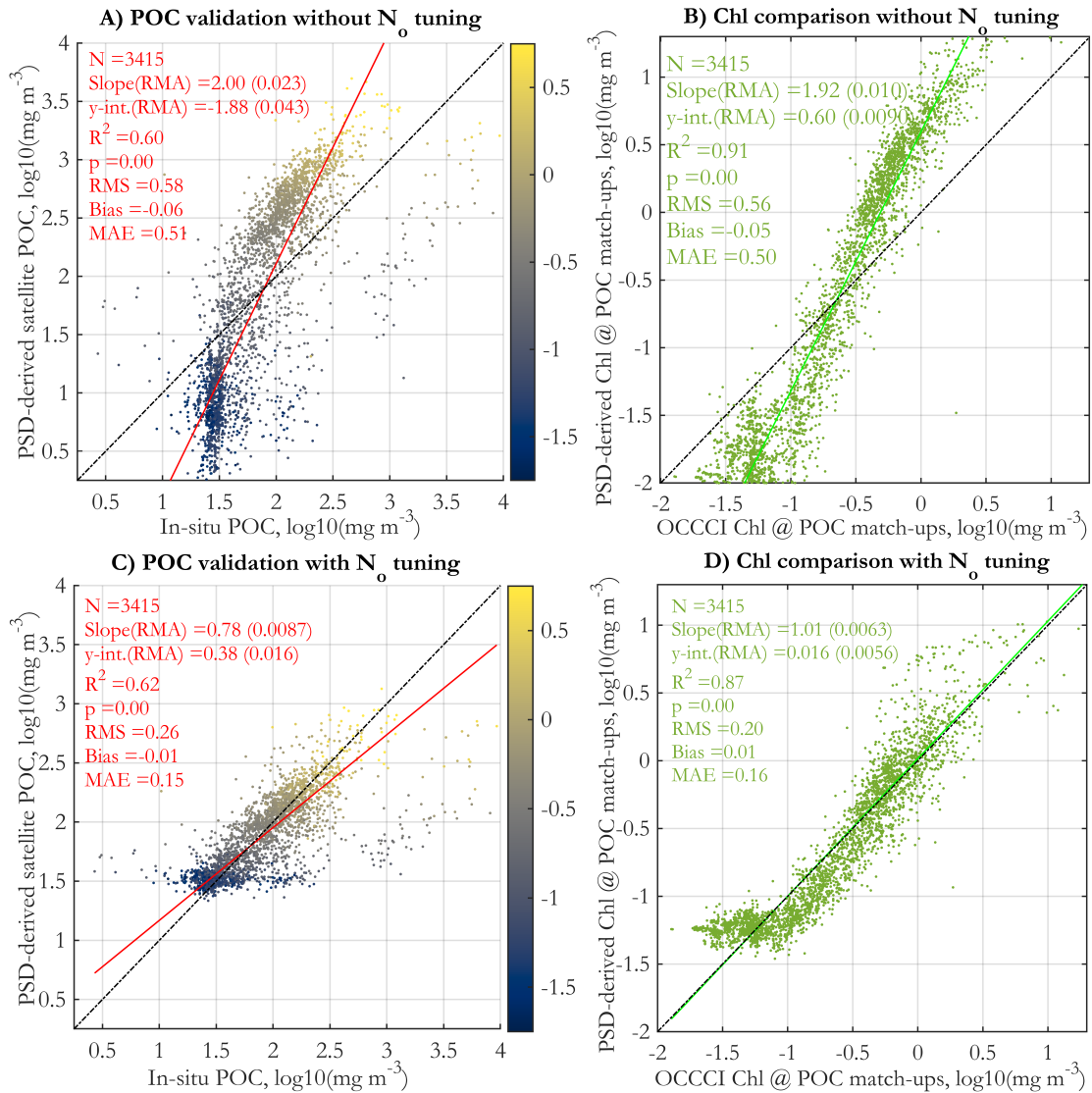
Figure 10. Validation of PSD-based POC retrievals vs. *in-situ* POC measurements, and comparison of satellite retrievals of Chl using the standard OC-CCI v5.0 algorithm vs. Chl estimated from the PSD. Panels (A) and (B) have no tuning applied, whereas empirical tuning is applied to the N_0 parameter (Eq. 7) for panels C and D. The tuning procedure applies a linear correction to N_0 in log10 space to ensure reasonable retrievals of POC and Chl, based on monthly satellite images from 2004 and 2015 - for details, see Supplement Sec. S5. The data points in panels A and C are colored by their matched standard OC-CCI v5.0 satellite Chl values (colormap, in $mg\,m^{-3}$ in log10 space).
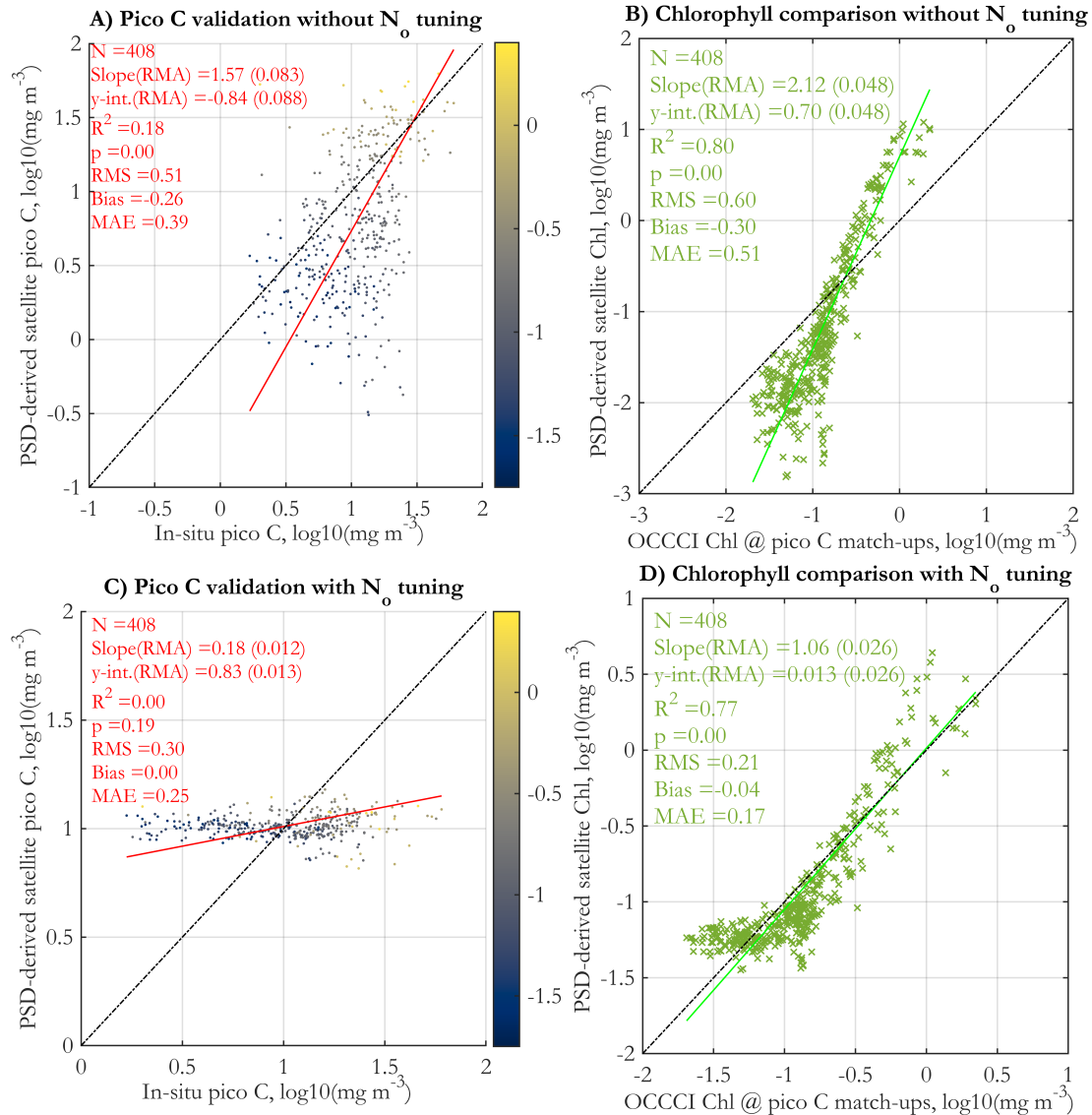
Figure 11. Validation of pico-phytoplankton carbon derived from the PSD model using daily OC-CCI v5.0 satellite data vs. *in-situ* measurements, as used in the POCO project (Martínez-Vicente et al., 2017) (panels A and C). Comparison of PSD-derived satellite Chl (y-axes) with the matched satellite retrieval of Chl using the standard OC-CCI v5.0 algorithm, at the locations of the *in-situ* pico-phytoplankton carbon match-up points (panels B and D). Panels (A) and (B) have no tuning applied, whereas empirical tuning is applied to the N_0 parameter (Eq. 7) for panels C and D. The tuning procedure applies a linear correction to N_0 in log10 space to ensure reasonable retrievals of POC and Chl, based on monthly satellite images from 2004 and 2015 - for details, see Supplement Sec. S5. The data points in panels A and C are colored by their matched standard OC-CCI v5.0 satellite Chl values (colormap, in $\mathrm{mg\,m^{-3}}$ in log10 space).

~~PSCs — differences in internal composition and structure, as well as shape, can be important too, and can significantly affect b_{bp} and the validation results.~~

3.4 Further Discussion, Summary, and Conclusions

The novel PSD/phyto C algorithm described here represents a major overhaul of the KSM09 algorithm (Kostadinov et al., 2009)
530 (a comparison between KSM09 and the present algorithm is briefly discussed in Supplement Sect. S6). Unlike KSM09, two distinct particle populations are used - phytoplankton and NAP. Phytoplankton backscattering is modeled using coated spheres Mie calculations with inputs based on the Equivalent Algal Populations (EAP) approach (Bernard et al., 2009; Robertson Lain and Bernard, 2018). This model formulation allows assessment of percent contribution of phytoplankton and NAP to total b_{bp}, as well as Chl to be estimated from the retrieved PSD. Underlying b_{bp} forward modeling is hyperspectral, facilitating adaptation
535 of the algorithm to upcoming hyperspectral sensors like PACE (Werdell et al., 2019). PSD retrieval is achieved via spectral angle mapping (SAM), and no spectral shape is imposed on b_{bp}; operational end-members for current and past multi-spectral sensors and the OC-CCI v5.0 merged ocean color data set are created via band-averaging from the underlying hyperspectral modeled b_{bp}.

The algorithm has been used to create an accompanying data set based on the OC-CCI v5.0 data set (~~See~~ Kostadinov et al. (2022)
540 , see Sec. 4).

We emphasize that the PSD parameters and derived retrievals presented here and in the accompanying data set (Kostadinov et al. (2022)) are an experimental, research satellite product with relatively large uncertainties. We do not claim that it is akin in validity and accuracy to the more established (and much more empirical!) algorithms for canonical products such as Chl and POC. As emphasized elsewhere in this text, the goal is to build an operational algorithm based on first principles as much as feasible, even
545 at the expense of accuracy, in order to push the boundaries of what is retrievable from space and move the science of bio-optical algorithm development forward. Potential users of these PSD and derived data (Kostadinov et al. (2022)) need to be aware of its limitations, uncertainties and validation status, before using them, for example, in building or validation/constraining biogeochemical models. The choice of IOP algorithm to retrieve $b_{bp}(\lambda)$ is key for the PSD/phyto C algorithm, as the spectral shape of b_{bp} is what the PSD slope retrieval is based upon (Eq. 4). The Loisel and Stramski (2000) IOP algorithm is chosen
550 here, as in KSM09, because it allows spectral b_{bp} retrievals that are not constrained by a specific spectral function or parameterization on b_{bp} as is done, for example, in QAA (Lee et al., 2002) and GSM (Maritorena et al., 2002, 2010). For the wavelengths used in the PSD slope retrieval, modeled and satellite-derived b_{bp} spectral shapes compare well when the Loisel and Stramski (2000) algorithm is used and global patterns of the retrieved PSD parameters appear reasonable. Preliminary tests with Loisel et al. (2018) indicate that this algorithm is not as suitable for PSD retrieval in this regard. Use of Loisel et al. (2018), Jorge
555 et al. (2021) and other IOP algorithms will be further investigated in future development of the PSD algorithm.

An important assumption of the model is that N_0 for NAP is twice that for phytoplankton, so that the phyto C to POC ratio is a constant 1:3. This ratio is expected to vary in the real ocean, and the value used here is a reasonable average choice (e.g. Behrenfeld et al. (2005); Jackson et al. (2017); Thomalla et al. (2017) and refs. therein). ~~Graff et al. (2012)~~ Graff et al. (2015) employed the cell sorting and chemical analysis methods of Graff et al. (2012) to measure phyto C in the Equatorial Pacific

 and along the Atlantic Meridional Transect (AMT). Their results indicate that a phyto C:POC value of 1/3 is reasonable, falling within their observed ranges; however, they do observe many higher values, particularly in the oligotrophic gyres. The Roy et al. (2017) phyto C to Stramski et al. (2008) POC ratio (applied to the May 2015 monthly image of the OC-CCI v5.0 data) indicates generally lower values of this ratio (with some high latitude and coastal exceptions), and even lower values occur in the gyres, with values mostly below 0.1 in the low-latitude open ocean (not shown). In light of this observation, note the

565 difference between the Graff et al. (2015) and Roy et al. (2017) phyto C retrievals (Fig. 9 and Supplement Fig. S8). Further direct analytical observations of phyto C and the reconciliation and better understanding of the spatio-temporal variability of the phyto C to POC ratio should be a high priority in order to improve understanding of carbon pools and their relationships in the ocean (Brewin et al., 2021) and ~~to~~ retrieve phyto C reliably from space.

~~When the modeled b_{bp} spectra (Fig. 2) are used to design look-up tables (LUTs)as in KSM09 (Kostadinov et al., 2009), one~~
570 ~~can compare the KSM09 algorithm to the model developed here. Results indicate that the LUTs relating the b_{bp} slope to the PSD slope are quite similar, differing by ≈ 0.2 (in PSD slope)at the most, when ξ values are from 3.5 to 4.0 (not shown). The LUTs practically coincide for very low and very high PSD slopes. LUTs of the new algorithm for the various sensors are very similar to each other. The LUTs linking the b_{bp} slope to the N_0 parameter for KSM09 and the new algorithm are also similar to first order (in logarithmic space). Importantly, the new algorithm LUTs (also nearly coinciding for the various sensors)~~
575 ~~indicate higher backscattering per particle for low~~ The relatively poor PSD parameter validation results should be interpreted with caution, as there are multiple reasons for discrepancies between the *in-situ* and satellite data and for the observed poor regression statistics, and the *in-situ* data have their own limitations. Importantly, the *in-situ* data PSD parameters are fit over a much narrower diameter range than the size range optically contributing the bulk of b_{bp} ~~slope values below ≈ 0.75 (typical for more eutrophic waters), and they indicate lower backscattering per particle for steeper backscattering spectral slopes (typical for~~
580 ~~more oligotrophic conditions). This can lead to up to a factor of ≈ 2 difference in retrieved~~ (e.g. see Supplement Fig. S4), at least according to the modeled spectra. It is recognized that in the real world the particle assemblage is very complex and its sources of backscattering are still not fully resolved (e.g. Stramski et al. (2004); Organelli et al. (2018)). In particular, the composition and PSD of small sub-micron particles appears to be of importance and is not well known; here we assume the same PSD and NAP composition across all size classes and globally. There is also a mismatch in temporal and spatial scales of sampling
585 between the satellite and *in-situ* data. For example, the matched *in-situ* PSD data do not exhibit the same negative correlation between ξ and N_0 that the satellite data do (Supplement Fig. S9). We note that this negative correlation in the satellite data has a theoretical underpinning because what we know about global ocean ecosystems, namely that oligotrophic areas exhibit relative dominance of smaller phytoplankton (and smaller overall concentrations of particles/biomass), as opposed to increased importance of larger phytoplankton and increased biomass in more eutrophic areas. We thus expect backscattering in the ocean
590 to become "bluer", i.e. to have a steeper spectral slope, in oligotrophic areas. This is indeed observed in satellite data (e.g. Loisel et al. (2006)) and is the basis for our algorithm. Therefore, we expect, in ~~particle concentrations retrieved. This LUT difference leads to a reduction of the apparent range exaggeration of retrieved phyto C globally (low values in~~ the ~~subtropical gyres, and high values in the eutrophic areas). It is this rangeexaggeration that led to the need for the empirical tuning in Kostadinov et al. (2016a). While the need for this tuning seems to persist for the new algorithm and is also implemented here~~

595 ~~(Sec. 3.3), validation and comparisons results here suggest that for some variables and algorithms being compared with,~~ ocean, globally and on average, N_0 to decrease with increasing ξ. This is not necessarily going to be captured by *in-situ* data of limited spatio-temporal coverage and fit over a narrower size range.

We further note that the ~~original version of~~ number of matched up sample points in the ~~novel PSD/phyto C algorithm performs better.~~

600 validation regression is different among PSD, POC and pico-phytoplankton C, and their geographic distribution is different as well (Supplement Fig. S5). Namely, there are about an order of magnitude more POC match-ups than pico-phytoplankton carbon ones. Thus the different validation results presented here do not necessarily represent the same oceanographic conditions, e.g. the pico-phytoplankton C *in-situ* data has less representation of eutrophic areas and spans a smaller range of Chl than the POC validation, with very few points exceeding Chl = 1.0 mg m^{-3} (cf. Fig. 10B and 11B). The pico-phytoplankton C data in

605 Martínez-Vicente et al. (2017) are derived from cell counts (abundance) converted to carbon using specific conversion factors for different species/groups. Namely, 60 fg C per cell was used for *Prochlorococcus*, 154 fg cell^{-1} - for *Synechococcus*, and 1319 fg cell^{-1} for pico-eukaryotes. This differs from the PSD-based phyto C retrieval algorithm in which the conversion is a function of cell volume and is continuous. For the allometric coefficients of Roy et al. (2017) used here, the equivalent conversion factor is ≈ 53 fg cell^{-1} for cells of the smallest diameter within the pico-phytoplankton range (0.5 µm), and is ≈ 1825

610 fg cell^{-1} for the largest diameter cells within the pico-phytoplankton range (2.0 µm), indicating first order consistency, but not full equivalency, with the methods of Martínez-Vicente et al. (2017).

The global relationships of the PSD parameters, derived PSD-based phyto C, and POC versus Chl for the May 2015 monthly image are illustrated in Supplement Fig. S10. Globally, as expected, there is a strong correlation of Chl with these variables, with increasing Chl associated with decreasing PSD slope, and increasing N_0, phyto C and POC. While the relationship is

615 strong, there is significant spread of the PSD parameters and phyto C data for a given Chl value, suggesting that there is added value in retrieving them separately, and that they should not all be treated as simply correlates of Chl. We note that there is a need for further investigation to avoid uniqueness of retrieval issues and degrees of freedom/independence issues, as well as more comprehensive and complete error propagation, since a lot of ecosystem properties are indeed correlated with Chl, and all these retrievals come from the same multispectral data.

620 The power law (Eq. 1) is a parameterization of real-world PSDs, and while there are theoretical underpinnings (e.g. West et al. (1997); Brown et al. (2004); Hatton et al. (2021)) and observations (e.g. ~~Quinones et al. (2003)~~Quinones et al. (2003); Buonassissi and Dier , see also refs. in Boss et al. (2001)) supporting its applicability, particularly over large size ranges, real-world PSDs may deviate from the power-law, especially in coastal zones (e.g. ~~Reynolds et al. (2010); Buonassissi and Dierssen (2010); Koestner et al. (2020)~~Reynolds et al. (2010); Koestner et al. (2020); Runyan et al. (2020); Reynolds and Stramski (2021)).There is less information

625 on living phytoplankton only, and their specific PSDs, because it has been historically difficult to separate living phytoplankton and measure, say, their PSD or carbon (e.g. (Graff et al., 2012, 2015)). A recent study by (Haëntjens et al., 2022) investigates phytoplankton specific PSDs; their observations support the conclusion that the phytoplankton-specific PSD shape is consistent with a power-law to first order. We note that phytoplankton share their size domain with other organisms (bacteria on the low end and zooplankton at the high end) and we note that a drop-off in the phytoplankton PSD will be expected at the limits of

630   the size range of autotrophs (e.g. see Hatton et al. (2021)) hence a phytoplankton-specific power-law will have upper and lower range limits of applicability, and it is not expected to apply equally well over the same size range everywhere and always in the global ocean. Hatton et al. (2021) offer an assessment of the PSD of marine life over a huge range of sizes (body mass), demonstrating that a specific power-law applies, in the context of the Sheldon et al. (1972) hypothesis that equal biomass tends to occur in each logarithmically-spaced size bin; their work offer support for use of the power-law for modeling phytoplankton

635   (over their size range) globally.

The power-law is not a converging PSD model, i.e. it is sensitive to the chosen limits of integration (for a sensitivity analysis to the integration limits, see Kostadinov et al. (2016a)). Gamma functions may be a better choice to represent marine PSDs (Risović, 1993; Risović, 2002). However, we choose to use the power-law because of its theoretical underpinnings and because the goal is to build an operational algorithm (based on first principles as much as possible) for existing multispectral data

640   with limited degrees of freedom. We additionally assume that the PSD slope for both phytoplankton and NAP is the same, limiting the number of parameters to be retrieved. Hyperspectral data and observations of phytoplankton and NAP-specific PSDs and IOPs will be needed to relax these assumptions in the future. Organelli et al. (2020) observed that the PSD slope steepened for small particles, deviating from a power-law. This steepening could partially explain the putative under-estimates of the original algorithm in oligotrophic gyres. Moreover, the absolute number of particles retrieved is sensitive to uncertainties

645   in the real index of refraction assumed. In this context, we note that the algorithm is able to pick up the concentration of particles, to first order, according to the N_0 validation (Fig. 8B). We find this to be impressive and consider it a success, given that the algorithm makes no *a-priori* prescriptions about particle concentrations – they are solved for from the magnitude and shape of satellite-observed b_{bp}. While the goal here is to create a global algorithm which uses one set of end-members, we recognize that future implementations can be improved by assessing the impact of using regionally variable subsets of index

650   of refraction distributions. The PSD parameterization and choices of Mie inputs, in particular complex indices of refraction, represent important sources of uncertainty and can also affect the need for tuning and the degree of suitability of estimating POC with our generic NAP population. Further algorithm analysis of performance and improvements need to focus on the index of refraction choices for the particle populations. For further discussion of algorithm uncertainties, see Kostadinov et al. (2009),Kostadinov et al. (2010) and Kostadinov et al. (2016a).

655   Graff et al. (2015) observe a relationship between phyto C and b_{bp} that is stronger than that for other proxies. This is encouraging for the use of backscattering as a proxy for phytoplankton carbon biomass. However, the link between the PSD and b_{bp} spectral shape is a second-order effect that is not easily observed in *in-situ* observations (Kostadinov et al., 2009; Slade and Boss, 2015; Org (Kostadinov et al., 2009; Slade and Boss, 2015; Boss et al., 2018; Organelli et al., 2020), even though theoretical modeling demonstrates a clear link (Kostadinov et al. (2009); this study). Kostadinov et al. (2012) discuss some reasons why it may be difficult

660   to observe this relationship in current *in-situ* data, e.g. the fact that the PSD is fit over a narrow range of diameters compared to the size range theoretically affecting b_{bp}. Nevertheless, these considerations and the overall performance of the KSM09 homogeneous algorithm as compared to the algorithm presented here leads to the conclusion that there are four primary directions that should be priorities for moving forward. First, investigate the effect of choices of index of refraction distributions, as discussed above. Second, rather than relying only on b_{bp} for PSD and phyto C retrieval, a blended approach should be developed

that also uses absorption, i.e. combine the approach here with that of Roy et al. (2017). Third, investigate the ability of hyperspectral data to provide more degrees of freedom for retrieval of more variables simultaneously, allowing relaxation of some key assumptions and perhaps a third particle population to represent POC and mineral particles separately; this is important in light of the upcoming PACE mission (Werdell et al., 2019). Hyperspectral absorption data in particular have the potential to increase information content and allow group-specific retrievals (e.g. Kramer et al. (2022), but see also Cael et al. (2020)). Finally, fourth, collect more global, comprehensive *in-situ* data sets of all relevant variables, including and especially of phyto C (Graff et al. (2015)), for further model development and validation. With regard to the latter, agencies and investigators should focus on building quality controlled, one-stop-shop data sets.

4   Additional Information

Code and data availability. Code and data associated with algorithm development, as well as operational application to OC-CCI v5.0 data are published on the Zenodo® repository (Kostadinov et al., 2022) and are available at the following URL: https://doi.org/10.5281/zenodo.6354654.

An OC-CCI v5.0-based satellite PSD/phyto C data set (monthly, 1997-2020, plus monthly and overall climatologies) has been published on the PANGAEA® repository (Kostadinov et al., 2022) and is freely available in netCDF format and browse images at the following URL: https://doi.org/10.1594/PANGAEA.939863

Appendix A: Details on the OC-CCI v5.0 Dataset

Processing and analysis was done using the sinusoidal projection of OC-CCI v5.0. For user convenience, once the final products were generated, they were re-projected to equidistant cylindrical projection (unprojected latitude/longitude) before publication to the data repository linked above (Sec. 4). The empirical tuning (Sec. 3.3) is not applied to the variables in the published data set (Sec. 4). Instead, the spatially-explicit linear-space multiplicative tuning factor (Supplement Fig. S7B) is given. The choice to provide an optional tuning to be applied at the user's discretion is dictated by the validation and comparison results discussed in the manuscript.

Author contributions. TSK designed the study, conducted the modeling and algorithm development and data analyses, and wrote the manuscript. SB and LRL provided the EAP model code and technical support for EAP modeling. SM helped with error propagation estimates and designed the band shifting methodology. CEK, BJ, VMV and SS extracted match ups and/or provided match up *in-situ* and satellite data set compilations. XZ provided the coated spheres code and technical support for it, as well as validation PSD data. HL and DSFJ provided technical assistance with IOP code testing. EK tested backscattering spectral shape sensitivity. SR provided Roy et al. (2017) algorithm output data. SB, LRL, XZ, SM, EK, SR, CEK, BJ, SS, HL, and DSFJ read the manuscript and provided comments/edits.

Competing interests. The authors declare no competing interests.

Disclaimer. The views and opinions expressed here are those of the authors and do not necessarily express those of NASA.

695   *Acknowledgements.* Funding for this project was provided by NASA grant #80NSSC19K0297 to TSK, Irina Marinov and SM. TSK also acknowledges support from California State University San Marcos. This work is a contribution to the Simons Foundation Project Computational Biogeochemical Modeling of Marine Ecosystems (CBIOMES, number 549947, S.S.). This paper is also a contribution to the ESA projects Ocean Colour Climate Change Initiative (OC-CCI) and the Biological Pump and Carbon Exchange Processes (BICEP). Additional support from the National Centre for Earth Observations (UK) is also gratefully acknowledged.

700   We acknowledge Olaf Hansen, Harish Vedantham, Marco Bellacicco, Salvatore Marullo, Irina Marinov, Ivona Cetinic, Giorgio Dall'Olmo and David Desailly for various help/useful discussions. We acknowledge the ESA OC-CCI and BICEP Project teams and contributors, *in-situ* PSD validation data contributors as given in Kostadinov et al. (2009) and David Siegel/ UCSB ERI / Plumes and Blooms Project team, the NASA EXPORTS and NAAMES cruises teams, and Giorgio Dall'Olmo, Emmanuele Organelli and the AMT26 cruise team for their in-situ PSD data (Organelli and Dall'Olmo, 2018). We acknowledge Emmanuel Boss and Nils Haëntjens for their *in-situ* PSD data and technical

705   help with it. We acknowledge all *in-situ* data contributors to the BICEP/POCO projects compilations of POC and pico-phytoplankton carbon data sets. The OC-CCI reference is Sathyendranath et al. (2019) and the v5.0 specific reference is Sathyendranath et al. (2021). The modeling and processing is done using the sinusoidal projection (one of the projections provided by OC-CCI), whereas maps here are presented in equidistant cylindrical projection (unprojected lat/lon). Erik Fields, ESA, BEAM (Brockmann Consult GmbH) and NASA are acknowledged for the re-projection algorithm. Coastlines in maps shown here are from v2.3.7 of the GSHHS data set - see Wessel and Smith (1996).

710   The NOAA ETOPO1 data set (https://www.ngdc.noaa.gov/mgg/global/ was used in validation for bathymetry masking. Modeling and data processing was done in MATLAB®.

The cividis colormap used in most visualizations is a variant of the viridis colormap optimized for color vision deficiency perception and is from Nuñez et al. (2018) and the function to implement it in MATLAB® is due to Ed Hawkins.

We acknowledge Emmanuel Boss and an anonymous reviewer for their very useful comments which helped improve the manuscript.

References

Aden, A. L. and Kerker, M.: Scattering of Electromagnetic Waves from Two Concentric Spheres, Journal of Applied Physics, 22, 1242–1246, https://doi.org/10.1063/1.1699834, 1951.

Babin, M., Morel, A., Fournier-Sicre, V., Fell, F., and Stramski, D.: Light scattering properties of marine particles in coastal and open ocean waters as related to the particle mass concentration, Limnology and Oceanography, 48, 843–859, https://doi.org/https://doi.org/10.4319/lo.2003.48.2.0843, 2003.

Bader, H.: The hyperbolic distribution of particle sizes, Journal of Geophysical Research (1896-1977), 75, 2822–2830, https://doi.org/10.1029/JC075i015p02822, 1970.

Behrenfeld, M. J., Boss, E., Siegel, D. A., and Shea, D. M.: Carbon-based ocean productivity and phytoplankton physiology from space, Global Biogeochemical Cycles, 19, 1–14, https://doi.org/10.1029/2004GB002299, 2005.

Bellacicco, M., Volpe, G., Briggs, N., Brando, V., Pitarch, J., Landolfi, A., Colella, S., Marullo, S., and Santoleri, R.: Global Distribution of Non-algal Particles From Ocean Color Data and Implications for Phytoplankton Biomass Detection, Geophysical Research Letters, 45, 7672–7682, https://doi.org/10.1029/2018GL078185, 2018.

Bernard, S., Probyn, T. A., and Quirantes, A.: Simulating the optical properties of phytoplankton cells using a two-layered spherical geometry, Biogeosciences Discussions, 6, 1497–1563, https://doi.org/10.5194/bgd-6-1497-2009, 2009.

Bohren, C. F. and Huffman, D. R. .: Absorption and Scattering of Light by Small Particles., Wiley, New York, 1983.

Boss, E., Twardowski, M. S., and Herring, S.: Shape of the particulate beam attenuation spectrum and its inversion to obtain the shape of the particulate size distribution, Appl. Opt., 40, 4885–4893, https://doi.org/10.1364/AO.40.004885, 2001.

Boss, E., Haëntjens, N., Westberry, T. K., Karp-Boss, L., and Slade, W. H.: Validation of the particle size distribution obtained with the laser in-situ scattering and transmission (LISST) meter in flow-through mode, Opt. Express, 26, 11 125–11 136, https://doi.org/10.1364/OE.26.011125, 2018.

Boyd, P. W., Claustre, H., Levy, M., Siegel, D. A., and Weber, T.: Multi-faceted particle pumps drive carbon sequestration in the ocean, Nature, 568, 327–335, https://doi.org/10.1038/s41586-019-1098-2, 2019.

Brewin, R. J., Sathyendranath, S., Platt, T., Bouman, H., Ciavatta, S., Dall'Olmo, G., Dingle, J., Groom, S., Jönsson, B., Kostadinov, T. S., Kulk, G., Laine, M., Martínez-Vicente, V., Psarra, S., Raitsos, D. E., Richardson, K., Rio, M. H., Rousseaux, C. S., Salisbury, J., Shutler, J. D., and Walker, P.: Sensing the ocean biological carbon pump from space: A review of capabilities, concepts, research gaps and future developments, Earth-Science Reviews, 217, https://doi.org/10.1016/j.earscirev.2021.103604, 2021.

Brown, J. H., Gillooly, J. F., Allen, A. P., Savage, V. M., and West, G. B.: TOWARD A METABOLIC THEORY OF ECOLOGY, Ecology, 85, 1771–1789, https://doi.org/10.1890/03-9000, 2004.

Buesseler, K. O. and Boyd, P. W.: Shedding light on processes that control particle export and flux attenuation in the twilight zone of the open ocean, Limnology and Oceanography, 54, 1210–1232, https://doi.org/10.4319/lo.2009.54.4.1210, 2009.

Buonassissi, C. J. and Dierssen, H. M.: A regional comparison of particle size distributions and the power law approximation in oceanic and estuarine surface waters, Journal of Geophysical Research: Oceans, 115, 1–12, https://doi.org/10.1029/2010JC006256, 2010.

Burd, A. B. and Jackson, G. A.: Particle Aggregation, Annual Review of Marine Science, 1, 65–90, https://doi.org/10.1146/annurev.marine.010908.163904, 2009.

Cael, B. B., Chase, A., and Boss, E.: Information content of absorption spectra and implications for ocean color inversion, Appl. Opt., 59, 3971–3984, https://doi.org/10.1364/AO.389189, 2020.

Chisholm, S. W.: Stirring times in the Southern Ocean, Nature, 407, 685–687, https://doi.org/10.1038/35037696, 2000.

Clavano, W., Boss, E., and Karp-Boss, L.: Inherent Optical Properties of Non-Spherical Marine-Like Particles ‚Äî From Theory To Observation, Oceanography and Marine Biology, pp. 1–38, https://doi.org/10.1201/9781420050943.ch1, 2007.

755   Dall'Olmo, G., Westberry, T. K., Behrenfeld, M. J., Boss, E., and Slade, W. H.: Significant contribution of large particles to optical backscattering in the open ocean, Biogeosciences, 6, 947–967, https://doi.org/10.5194/bg-6-947-2009, 2009.

Dennison, P. E., Halligan, K. Q., and Roberts, D. A.: A comparison of error metrics and constraints for multiple endmember spectral mixture analysis and spectral angle mapper, Remote Sensing of Environment, 93, 359–367, https://doi.org/10.1016/j.rse.2004.07.013, 2004.

Duforêt-Gaurier, L., Dessailly, D., Moutier, W., and Loisel, H.: Assessing the impact of a two-layered spherical geometry of phytoplankton

760   cells on the bulk backscattering ratio of marine particulate matter, Applied Sciences (Switzerland), 8, https://doi.org/10.3390/app8122689, 2018.

Eppley, R. W. and Peterson, B. J.: Particulate organic matter flux and planktonic new production in the deep ocean, Nature, 282, 677–680, 1979.

Evers-King, H., Martinez-Vicente, V., Brewin, R. J. W., Dall'Olmo, G., Hickman, A. E., Jackson, T., Kostadinov, T. S., Krasemann,

765   H., Loisel, H., Röttgers, R., Roy, S., Stramski, D., Thomalla, S., Platt, T., and Sathyendranath, S.: Validation and Intercomparison of Ocean Color Algorithms for Estimating Particulate Organic Carbon in the Oceans, Frontiers in Marine Science, 4, 1–20, https://doi.org/10.3389/fmars.2017.00251, 2017.

Falkowski, P. G., Barber, R. T., and Smetacek, V.: Biogeochemical controls and feedbacks on ocean primary production, Science, 281, 200–206, https://doi.org/10.1126/science.281.5374.200, 1998.

770   Field, C. B., Behrenfeld, M. J., Randerson, J. T., and Falkowski, P.: Primary production of the biosphere: Integrating terrestrial and oceanic components, Science, 281, 237–240, https://doi.org/10.1126/science.281.5374.237, 1998.

Graff, J. R., Milligan, A. J., and Behrenfeld, M. J.: The measurement of phytoplankton biomass using flow-cytometric sorting and elemental analysis of carbon, Limnology and Oceanography: Methods, 10, 910–920, https://doi.org/10.4319/lom.2012.10.910, 2012.

Graff, J. R., Westberry, T. K., Milligan, A. J., Brown, M. B., Dall'Olmo, G., van Dongen-Vogels, V., Reifel, K. M., and Behrenfeld, M. J.:

775   Analytical phytoplankton carbon measurements spanning diverse ecosystems, Deep-Sea Research Part I: Oceanographic Research Papers, 102, 16–25, https://doi.org/10.1016/j.dsr.2015.04.006, 2015.

Hatton, I. A., Heneghan, R. F., Bar-On, Y. M., and Galbraith, E. D.: The global ocean size spectrum from bacteria to whales, Science Advances, 7, 1–13, https://doi.org/10.1126/sciadv.abh3732, 2021.

Haëntjens, N., Boss, E. S., Graff, J. R., Chase, A. P., and Karp-Boss, L.: Phytoplankton size distributions in the western North Atlantic and

780   their seasonal variability, Limnology and Oceanography, 67, 1865–1878, https://doi.org/https://doi.org/10.1002/lno.12172, 2022.

Henson, S. A., Sanders, R., Madsen, E., Morris, P. J., Le Moigne, F., and Quartly, G. D.: A reduced estimate of the strength of the ocean's biological carbon pump, Geophysical Research Letters, 38, 10–14, https://doi.org/10.1029/2011GL046735, 2011.

Jackson, T., Sathyendranath, S., and Platt, T.: An exact solution for modeling photoacclimation of the carbon-to-chlorophyll ratio in phytoplankton, Frontiers in Marine Science, 4, 1–10, https://doi.org/10.3389/fmars.2017.00283, 2017.

785   Jonasz, M.: Particle-size distributions in the Baltic, Tellus B: Chemical and Physical Meteorology, 35, 346–358, https://doi.org/10.3402/tellusb.v35i5.14624, 1983.

Jorge, D. S., Loisel, H., Jamet, C., Dessailly, D., Demaria, J., Bricaud, A., Maritorena, S., Zhang, X., Antoine, D., Kutser, T., Bélanger, S., Brando, V. O., Werdell, J., Kwiatkowska, E., Mangin, A., and d'Andon, O. F.: A three-step semi analytical algorithm (3SAA) for estimating

inherent optical properties over oceanic, coastal, and inland waters from remote sensing reflectance, Remote Sensing of Environment, 263,
https://doi.org/10.1016/j.rse.2021.112537, 2021.

Koestner, D., Stramski, D., and Reynolds, R. A.: Assessing the effects of particle size and composition on light scattering through measurements of size-fractionated seawater samples, Limnology and Oceanography, 65, 173–190, https://doi.org/10.1002/lno.11259, 2020.

Kostadinov, T., Siegel, D., Maritorena, S., and Guillocheau, N.: Ocean color observations and modeling for an optically complex site: Santa Barbara Channel, California, USA, Journal of Geophysical Research: Oceans, 112, https://doi.org/10.1029/2006JC003526, 2007.

Kostadinov, T., Siegel, D., and Maritorena, S.: Retrieval of the particle size distribution from satellite ocean color observations, Journal of Geophysical Research: Oceans, 114, https://doi.org/10.1029/2009JC005303, 2009.

Kostadinov, T., Siegel, D., and Maritorena, S.: Global variability of phytoplankton functional types from space: Assessment via the particle size distribution, Biogeosciences, 7, https://doi.org/10.5194/bg-7-3239-2010, 2010.

Kostadinov, T., Siegel, D., Maritorena, S., and Guillocheau, N.: Optical assessment of particle size and composition in the Santa Barbara Channel, California, Applied Optics, 51, https://doi.org/10.1364/AO.51.003171, 2012.

Kostadinov, T., Milutinovic, S., Marinov, I., and Cabré, A.: Carbon-based phytoplankton size classes retrieved via ocean color estimates of the particle size distribution, Ocean Science, 12, https://doi.org/10.5194/os-12-561-2016, 2016a.

Kostadinov, T. S., Milutinovic, S., Marinov, I., and Cabré, A.: Size-partitioned phytoplankton carbon concentrations retrieved from ocean color data, links to data in NetCDF format, https://doi.org/10.1594/PANGAEA.859005, 2016b.

Kostadinov, T. S., Roberston-Lain, L., Bernard, S., Zhang, X., and Loisel, H.: PSD_PhytoC_v2021: Ocean Color Algorithm for the Retrieval of the Particle Size Distribution and Size-Partitioned Phytoplankton Carbon: Algorithm Development and Operational Code, https://doi.org/10.5281/zenodo.6354654, 2022.

Kostadinov, T. S., Robertson-Lain, L., Kong, C. E., Zhang, X., Maritorena, S., Bernard, S., Loisel, H., Jorge, D. S. F., Kochetkova, E., Roy, S., Jönsson, B., Martinez-Vicente, V., and Sathyendranath, S.: Particle Size Distribution and Size-partitioned Phytoplankton Carbon Using a Two-Component Coated-Spheres Bio-optical Model: Monthly Global 4 km Imagery Based on the OC-CCI v5.0 Merged Ocean Color Sat, https://doi.org/10.1594/PANGAEA.939863, 2022.

Kramer, S. J., Siegel, D. A., Maritorena, S., and Catlett, D.: Modeling surface ocean phytoplankton pigments from hyperspectral remote sensing reflectance on global scales, Remote Sensing of Environment, 270, https://doi.org/10.1016/j.rse.2021.112879, 2022.

Lee, Z., Carder, K. L., and Arnone, R. A.: Deriving inherent optical properties from water color: a multiband quasi-analytical algorithm for optically deep waters, Applied Optics, 41, 5755, https://doi.org/10.1364/AO.41.005755, 2002.

Lee, Z. P., Carder, K., Arnone, R., and He, M. X.: Determination of primary spectral bands for remote sensing of aquatic environments, Sensors, 7, 3428–3441, https://doi.org/10.3390/s7123428, 2007.

Loisel, H. and Stramski, D.: Estimation of the inherent optical properties of natural waters from the irradiance attenuation coefficient and reflectance in the presence of Raman scattering, Appl. Opt., 39, 3001–3011, https://doi.org/10.1364/AO.39.003001, 2000.

Loisel, H., Nicolas, J. M., Sciandra, A., Stramski, D., and Poteau, A.: Spectral dependency of optical backscattering by marine particles from satellite remote sensing of the global ocean, Journal of Geophysical Research: Oceans, 111, 1–14, https://doi.org/10.1029/2005JC003367, 2006.

Loisel, H., Stramski, D., Dessailly, D., Jamet, C., Li, L., and Reynolds, R. A.: An Inverse Model for Estimating the Optical Absorption and Backscattering Coefficients of Seawater From Remote-Sensing Reflectance Over a Broad Range of Oceanic and Coastal Marine Environments, Journal of Geophysical Research: Oceans, 123, 2141–2171, https://doi.org/10.1002/2017JC013632, 2018.

Marañón, E.: Cell Size as a Key Determinant of Phytoplankton Metabolism and Community Structure, Annual Review of Marine Science, 7, 241–264, https://doi.org/10.1146/annurev-marine-010814-015955, 2015.

Maritorena, S., Siegel, D. A., and Peterson, A. R.: Optimization of a semianalytical ocean color model for global-scale applications, Applied Optics, 41, 2705, https://doi.org/10.1364/AO.41.002705, 2002.

830 Maritorena, S., d'Andon, O. H. F., Mangin, A., and Siegel, D. A.: Merged satellite ocean color data products using a bio-optical model: Characteristics, benefits and issues, Remote Sensing of Environment, 114, 1791–1804, https://doi.org/10.1016/j.rse.2010.04.002, 2010.

Martínez-Vicente, V., Evers-King, H., Roy, S., Kostadinov, T., Tarran, G., Graff, J., Brewin, R., Dall'Olmo, G., Jackson, T., Hickman, A., Röttgers, R., Krasemann, H., Marañón, E., Platt, T., and Sathyendranath, S.: Intercomparison of ocean color algorithms for picophytoplankton carbon in the ocean, Frontiers in Marine Science, 4, https://doi.org/10.3389/fmars.2017.00378, 2017.

835 Menden-Deuer, S. and Lessard, E. J.: Carbon to volume relationships for dinoflagellates, diatoms, and other protist plankton, Limnology and Oceanography, 45, 569–579, https://doi.org/10.4319/lo.2000.45.3.0569, 2000.

Mie, G.: Beiträge zur Optik trüber Medien, speziell kolloidaler Metallösungen, Annalen der Physik, 330, 377–445, https://doi.org/10.1002/andp.19083300302, 1908.

Mobley, C. D., Sundman, L. K., and Boss, E.: Phase function effects on oceanic light fields, Applied Optics, 41, 1035, 840 https://doi.org/10.1364/ao.41.001035, 2002.

Morel, A. and Bricaud, A.: Inherent properties of algal cells including picoplankton: theoretical and experimental results, Canadian Bulletin of Fisheries and Aquatic Sciences, 214, 521–559, 1986.

Morel, A. and Maritorena, S.: Bio-optical properties of oceanic waters: A reappraisal, Journal of Geophysical Research, 106, 7163–7180, https://doi.org/10.1029/2000JC000319, 2001.

845 Morel, A., Yu-Hwan Ahn, Partensky, F., Vaulot, D., and Claustre, H.: Prochlorococcus and Synechococcus: a comparative study of their optical properties in relation to their size and pigmentation, Journal of Marine Research, 51, 617–649, https://doi.org/10.1357/0022240933223963, 1993.

Moutier, W., Duforêt-Gaurier, L., Thyssen, M., Loisel, H., Mériaux, X., Courcot, L., Dessailly, D., and Alvain, S.: Scattering of individual particles from cytometry: tests on phytoplankton cultures, Opt. Express, 24, 24 188–24 212, https://doi.org/10.1364/OE.24.024188, 2016.

850 Mouw, C. B., Hardman-mountford, N. J., Alvain, S., Bracher, A., Brewin, R. W., Bricaud, A., Ciotti, A. M., Devred, E., Hirata, T., Hirawake, T., Kostadinov, T. S., Roy, S., and Uitz, J.: A Consumer's Guide to Satellite Remote Sensing of Multiple Phytoplankton Groups in the Global Ocean, Frontiers in Marine Science, 4, https://doi.org/10.3389/fmars.2017.00041, 2017.

Nuñez, J. R., Anderton, C. R., and Renslow, R. S.: Optimizing colormaps with consideration for color vision deficiency to enable accurate interpretation of scientific data, PLOS ONE, 13, 1–14, https://doi.org/10.1371/journal.pone.0199239, 2018.

855 Organelli, E. and Dall'Olmo, G.: Particle size distributions in the upper 500 m of the Atlantic Ocean from the Atlantic Meridional Transect cruise AMT26 (JR16001) using a Coulter counter., https://doi.org/10.5285/79103bda-8913-39f3-e053-6c86abc0567a, 2018.

Organelli, E., Dall'Olmo, G., Brewin, R. J., Tarran, G. A., Boss, E., and Bricaud, A.: The open-ocean missing backscattering is in the structural complexity of particles, Nature Communications, 9, https://doi.org/10.1038/s41467-018-07814-6, 2018.

Organelli, E., Dall'Olmo, G., Brewin, R. J. W., Nencioli, F., and Tarran, G. A.: Drivers of spectral optical scattering by particles in the upper 860 500 m of the Atlantic Ocean, Optics Express, 28, 34 147, https://doi.org/10.1364/oe.408439, 2020.

Quéré, C. L., Harrison, S. P., Colin Prentice, I., Buitenhuis, E. T., Aumont, O., Bopp, L., Claustre, H., Cotrim Da Cunha, L., Geider, R., Giraud, X., Klaas, C., Kohfeld, K. E., Legendre, L., Manizza, M., Platt, T., Rivkin, R. B., Sathyendranath, S., Uitz, J., Watson, A. J., and

Wolf-Gladrow, D.: Ecosystem dynamics based on plankton functional types for global ocean biogeochemistry models, Global Change Biology, 11, 2016–2040, https://doi.org/10.1111/j.1365-2486.2005.1004.x, 2005.

865 Quinones, R. A., Platt, T., and Rodríguez, J.: Patterns of biomass-size spectra from oligotrophic waters of the Northwest Atlantic, Progress in Oceanography, 57, 405–427, https://doi.org/10.1016/S0079-6611(03)00108-3, plankton size-classes, functional groups and ecosystem dynamics, 2003.

Quirantes, A. and Bernard, S.: Light scattering by marine algae: Two-layer spherical and nonspherical models, Journal of Quantitative Spectroscopy and Radiative Transfer, 89, 311–321, https://doi.org/10.1016/j.jqsrt.2004.05.031, 2004.

870 Quirantes, A. and Bernard, S.: Light-scattering methods for modelling algal particles as a collection of coated and/or nonspherical scatterers, Journal of Quantitative Spectroscopy and Radiative Transfer, 100, 315–324, https://doi.org/10.1016/j.jqsrt.2005.11.048, 2006.

Reynolds, R. A. and Stramski, D.: Variability in Oceanic Particle Size Distributions and Estimation of Size Class Contributions Using a Non-parametric Approach, Journal of Geophysical Research: Oceans, 126, e2021JC017 946, https://doi.org/https://doi.org/10.1029/2021JC017946, e2021JC017946 2021JC017946, 2021.

875 Reynolds, R. A., Stramski, D., Wright, V. M., and Woźniak, S. B.: Measurements and characterization of particle size distributions in coastal waters, Journal of Geophysical Research: Oceans, 115, https://doi.org/10.1029/2009JC005930, 2010.

Risović, D.: Effect of suspended particulate-size distribution on the backscattering ratio in the remote sensing of seawater, Appl. Opt., 41, 7092–7101, https://doi.org/10.1364/AO.41.007092, 2002.

Risović, D.: Two-component model of sea particle size distribution, Deep Sea Research Part I: Oceanographic Research Papers, 40, 1459–
880 1473, https://doi.org/10.1016/0967-0637(93)90123-K, 1993.

Robertson Lain, L. and Bernard, S.: The fundamental contribution of phytoplankton spectral scattering to ocean colour: Implications for satellite detection of phytoplankton community structure, Applied Sciences (Switzerland), 8, 1–34, https://doi.org/10.3390/app8122681, 2018.

Robertson Lain, L., Bernard, S., and Evers-King, H.: Biophysical modelling of phytoplankton communities from first principles using two-
885 layered spheres: Equivalent Algal Populations (EAP) model, Optics Express, 22, 16 745, https://doi.org/10.1364/oe.22.016745, 2014.

Roy, S., Sathyendranath, S., Bouman, H., and Platt, T.: The global distribution of phytoplankton size spectrum and size classes from their light-absorption spectra derived from satellite data, Remote Sensing of Environment, 139, 185–197, https://doi.org/10.1016/j.rse.2013.08.004, 2013.

Roy, S., Sathyendranath, S., and Platt, T.: Size-partitioned phytoplankton carbon and carbon-to-chlorophyll ratio from ocean colour by an
890 absorption-based bio-optical algorithm, Remote Sensing of Environment, 194, 177–189, https://doi.org/10.1016/j.rse.2017.02.015, 2017.

Runyan, H., Reynolds, R. A., and Stramski, D.: Evaluation of Particle Size Distribution Metrics to Estimate the Relative Contributions of Different Size Fractions Based on Measurements in Arctic Waters, Journal of Geophysical Research: Oceans, 125, e2020JC016 218, https://doi.org/https://doi.org/10.1029/2020JC016218, e2020JC016218 2020JC016218, 2020.

Sathyendranath, S., Brewin, R. J., Brockmann, C., Brotas, V., Calton, B., Chuprin, A., Cipollini, P., Couto, A. B., Dingle, J., Doerffer,
895 R., Donlon, C., Dowell, M., Farman, A., Grant, M., Groom, S., Horseman, A., Jackson, T., Krasemann, H., Lavender, S., Martinez-Vicente, V., Mazeran, C., Mélin, F., Moore, T. S., Müller, D., Regner, P., Roy, S., Steele, C. J., Steinmetz, F., Swinton, J., Taberner, M., Thompson, A., Valente, A., Zühlke, M., Brando, V. E., Feng, H., Feldman, G., Franz, B. A., Frouin, R., Gould, R. W., Hooker, S. B., Kahru, M., Kratzer, S., Mitchell, B. G., Muller-Karger, F. E., Sosik, H. M., Voss, K. J., Werdell, J., and Platt, T.: An ocean-colour time series for use in climate studies: The experience of the ocean-colour climate change initiative (OC-CCI), Sensors (Switzerland), 19,
900 https://doi.org/10.3390/s19194285, 2019.

Sathyendranath, S., Platt, T., Kovač, Ž., Dingle, J., Jackson, T., Brewin, R. J. W., Franks, P., Marañón, E., Kulk, G., and Bouman, H. A.: Reconciling models of primary production and photoacclimation [Invited], Applied Optics, 59, C100, https://doi.org/10.1364/ao.386252, 2020.

Sathyendranath, S., Jackson, T., Brockmann, C., Brotas, V., Calton, B., Chuprin, A., Clements, O., Cipollini, P., Danne, O., Dingle, J., Donlon, C., Grant, M., Groom, S., Krasemann, H., Lavender, S., Mazeran, C., Mélin, F., Műller, D., Steinmetz, F., Valente, A., Zűhlke, M., Feldman, G., Franz, B., Frouin, R., Werdell, J., and Platt, T.: ESA Ocean Colour Climate Change Initiative (Ocean_Colour_cci): Version 5.0 Data. NERC EDS Centre for Environmental Data Analysis, https://doi.org/10.5285/1dbe7a109c0244aaad713e078fd3059a, 2021.

Seegers, B. N., Stumpf, R. P., Schaeffer, B. A., Loftin, K. A., and Werdell, P. J.: Performance metrics for the assessment of satellite data products: an ocean color case study, Optics Express, 26, 7404, https://doi.org/10.1364/oe.26.007404, 2018.

Sheldon, R. W., Prakash, A., and Sutcliffe Jr., W. H.: THE SIZE DISTRIBUTION OF PARTICLES IN THE OCEAN1, Limnology and Oceanography, 17, 327–340, https://doi.org/10.4319/lo.1972.17.3.0327, 1972.

Siegel, D. A., Behrenfeld, M. J., Maritorena, S., McClain, C. R., Antoine, D., Bailey, S. W., Bontempi, P. S., Boss, E. S., Dierssen, H. M., Doney, S. C., Eplee, R. E., Evans, R. H., Feldman, G. C., Fields, E., Franz, B. A., Kuring, N. A., Mengelt, C., Nelson, N. B., Patt, F. S., Robinson, W. D., Sarmiento, J. L., Swan, C. M., Werdell, P. J., Westberry, T. K., Wilding, J. G., and Yoder, J. A.: Regional to global assessments of phytoplankton dynamics from the SeaWiFS mission, Remote Sensing of Environment, 135, 77–91, https://doi.org/10.1016/j.rse.2013.03.025, 2013.

Siegel, D. A., Buesseler, K. O., Doney, S. C., Sailley, S. F., Behrenfeld, M. J., and Boyd, P. W.: Global assessment of ocean carbon export by combining satellite observations and food-web models, Global Biogeochemical Cycles, 28, 181–196, https://doi.org/10.1002/2013GB004743, 2014.

Siegel, D. A., Buesseler, K. O., Behrenfeld, M. J., Benitez-nelson, C. R., Boss, E., Brzezinski, M. A., Burd, A., Carlson, C. A., Asaro, E. A. D., Doney, S. C., Perry, M. J., Stanley, R. H. R., and Steinberg, D. K.: Prediction of the Export and Fate of Global Ocean Net Primary Production : The EXPORTS Science Plan, Frontiers in Marine Science, 3, 1–10, https://doi.org/10.3389/fmars.2016.00022, 2016.

Siegel, D. A., Cetinić, I., Graff, J. R., Lee, C. M., Nelson, N., Perry, M. J., Ramos, I. S., Steinberg, D. K., Buesseler, K., Hamme, R., Fassbender, A. J., Nicholson, D., Omand, M. M., Robert, M., Thompson, A., Amaral, V., Behrenfeld, M., Benitez-Nelson, C., Bisson, K., Boss, E., Boyd, P. W., Brzezinski, M., Buck, K., Burd, A., Burns, S., Caprara, S., Carlson, C., Cassar, N., Close, H., D'Asaro, E., Durkin, C., Erickson, Z., Estapa, M. L., Fields, E., Fox, J., Freeman, S., Gifford, S., Gong, W., Gray, D., Guidi, L., Haëntjens, N., Halsey, K., Huot, Y., Hansell, D., Jenkins, B., Karp-Boss, L., Kramer, S., Lam, P., Lee, J. M., Maas, A., Marchal, O., Marchetti, A., McDonnell, A., McNair, H., Menden-Deuer, S., Morison, F., Niebergall, A. K., Passow, U., Popp, B., Potvin, G., Resplandy, L., Roca-Martí, M., Roesler, C., Rynearson, T., Traylor, S., Santoro, A., Seraphin, K. D., Sosik, H. M., Stamieszkin, K., Stephens, B., Tang, W., van Mooy, B., Xiong, Y., and Zhang, X.: An operational overview of the EXport processes in the ocean from RemoTe sensing (EXPORTS) northeast pacific field deployment, Elementa, 9, 1–31, https://doi.org/10.1525/elementa.2020.00107, 2021.

Slade, W. H. and Boss, E.: Spectral attenuation and backscattering as indicators of average particle size, Applied Optics, 54, 7264, https://doi.org/10.1364/ao.54.007264, 2015.

Stemmann, L. and Boss, E.: Plankton and Particle Size and Packaging: From Determining Optical Properties to Driving the Biological Pump, Annual Review of Marine Science, 4, 263–290, https://doi.org/10.1146/annurev-marine-120710-100853, 2012.

Stramski, D. and Kiefer, D. A.: Light scattering by microorganisms in the open ocean, Progress in Oceanography, 28, 343–383, https://doi.org/10.1016/0079-6611(91)90032-H, 1991.

Stramski, D., Bricaud, A., and Morel, A.: Modeling the inherent optical properties of the ocean based on the detailed composition of the planktonic community, Applied Optics, 40, 2929, https://doi.org/10.1364/ao.40.002929, 2001.

Stramski, D., Boss, E., Bogucki, D., and Voss, K. J.: The role of seawater constituents in light backscattering in the ocean, Progress in Oceanography, 61, 27–56, https://doi.org/10.1016/j.pocean.2004.07.001, 2004.

Stramski, D., Reynolds, R. A., Babin, M., Kaczmarek, S., Lewis, M. R., Röttgers, R., Sciandra, A., Stramska, M., Twardowski, M. S., Franz, B. A., and Claustre, H.: Relationships between the surface concentration of particulate organic carbon and optical properties in the eastern South Pacific and eastern Atlantic Oceans, Biogeosciences, 5, 171–201, https://doi.org/10.5194/bg-5-171-2008, 2008.

Thomalla, S. J., Ogunkoya, A. G., Vichi, M., and Swart, S.: Using optical sensors on gliders to estimate phytoplankton carbon concentrations and chlorophyll-to-carbon ratios in the Southern Ocean, Frontiers in Marine Science, 4, 1–19, https://doi.org/10.3389/FMARS.2017.00034, 2017.

Toole, D. A. and Siegel, D. A.: Modes and mechanisms of ocean color variability in the Santa Barbara Channel, Journal of Geophysical Research: Oceans, 106, 26 985–27 000, https://doi.org/10.1029/2000JC000371, 2001.

Twardowski, M. S., Boss, E., Macdonald, J. B., Pegau, W. S., Barnard, A. H., and Zaneveld, J. R. V.: A model for estimating bulk refractive index from the optical backscattering ratio and the implications for understanding particle composition in case I and case II waters, Journal of Geophysical Research: Oceans, 106, 14 129–14 142, https://doi.org/10.1029/2000jc000404, 2001.

van de Hulst, H. C.: Light scattering by small particles., Dover Publications, New York, 1981.

Vidondo, B., Prairie, Y. T., Blanco, J. M., and Duarte, C. M.: Some aspects of the analysis of size spectra in aquatic ecology, Limnology and Oceanography, 42, 184–192, https://doi.org/10.4319/lo.1997.42.1.0184, 1997.

Werdell, P. J., Behrenfeld, M. J., Bontempi, P. S., Boss, E., Cairns, B., Davis, G. T., Franz, B. A., Gliese, U. B., Gorman, E. T., Hasekamp, O., Knobelspiesse, K. D., Mannino, A., Martins, J. V., McClain, C. R., Meister, G., and Remer, L. A.: The plankton, aerosol, cloud, ocean ecosystem mission status, science, advances, Bulletin of the American Meteorological Society, 100, 1775–1794, https://doi.org/10.1175/BAMS-D-18-0056.1, 2019.

Wessel, P. and Smith, W. H.: A global, self-consistent, hierarchical, high-resolution shoreline database, Journal of Geophysical Research B: Solid Earth, 101, 8741–8743, https://doi.org/10.1029/96jb00104, 1996.

West, G. B., Brown, J. H., and Enquist, B. J.: A general model for the origin of allometric scaling laws in biology, Science, 276, 122–126, https://doi.org/10.1126/science.276.5309.122, 1997.

Woźniak, S. B. and Stramski, D.: Modeling the optical properties of mineral particles suspended in seawater and their influence on ocean reflectance and chlorophyll estimation from remote sensing algorithms, Appl. Opt., 43, 3489–3503, https://doi.org/10.1364/AO.43.003489, 2004.

Zhang, X., Lewis, M., Lee, M., Johnson, B., and Korotaev, G.: The volume scattering function of natural bubble populations, Limnology and Oceanography, 47, 1273–1282, https://doi.org/10.4319/lo.2002.47.5.1273, 2002.

Zhang, X., Hu, L., and He, M.-X.: Scattering by pure seawater: Effect of salinity, Opt. Express, 17, 5698–5710, https://doi.org/10.1364/OE.17.005698, 2009.

Zhang, X., Twardowski, M., and Lewis, M.: Retrieving composition and sizes of oceanic particle subpopulations from the volume scattering function, Appl. Opt., 50, 1240–1259, https://doi.org/10.1364/AO.50.001240, 2011.

Zhang, X., Gray, D. J., Huot, Y., You, Y., and Bi, L.: Comparison of optically derived particle size distributions: scattering over the full angular range versus diffraction at near forward angles, Appl. Opt., 51, 5085–5099, https://doi.org/10.1364/AO.51.005085, 2012.

Zhang, X., Hu, L., Xiong, Y., Huot, Y., and Gray, D.: Experimental Estimates of Optical Backscattering Associated With Submicron Particles in Clear Oceanic Waters, Geophysical Research Letters, 47, e2020GL087 100, https://doi.org/10.1029/2020GL087100, e2020GL087100 2020GL087100, 2020.

Supplement to "Ocean Color Algorithm for the Retrieval of the Particle Size Distribution and Carbon-Based Phytoplankton Size Classes Using a Two-Component Coated-Spheres Backscattering Model"

Tihomir S. Kostadinov et al.

S1 Assessment and propagation of uncertainties

The Monte Carlo simulations (N=3000) of the two-population Mie scattering model were used to estimate uncertainty of the retrieved PSD parameters that is due to assumptions of the values of the model input parameters. The input distributions from which the varying input parameters were sampled for the Monte Carlo simulations are shown in main text Tables 1 and 2. This approach resulted in 3000 different realizations of modeled spectral b_{bp}, for each ξ input value. The median of all realizations is used as the SAM end-members, and Kruskal-Wallis analysis of variance is used to determine class similarity (where each input ξ value represents a class). This analysis determined, for each class, the neighboring classes that are statistically not different from it (at the 5% significance level) in terms of spectral angle. This gave a range of possible retrieved ξ values. This range is not always symmetric, but it is approximated as a symmetric 95% confidence interval (CI) and converted to standard deviation for use in subsequent analytical error propagation. The standard deviation of the corresponding N_0 parameter across all similar classes and all Monte Carlo realizations is used as the uncertainty estimate for N_0.

The uncertainties of the PSD parameters and allometric coefficients were used with the first order derivatives of the derived products (absolute and fractional size-partitioned phyto C) with respect to those variables to analytically propagate the uncertainty estimate to the derived products. Phyto C absolute values are functions of both PSD parameters and both allometric coefficients, whereas the fractional values are functions only of ξ and the b allometric coefficient because a ratio of phyto C values is taken (Eq. 5). We use the allometric coefficients obtained by Roy et al. (2017), who use information from three different regressions presented in Menden-Deuer and Lessard (2000). The weighted mean of the confidence intervals of the Menden-Deuer and Lessard (2000) allometric coefficients was used. Uncertainties were also propagated analytically to the composite imagery (monthly and overall climatologies) provided in the OC-CCI-derived PSD/phyto C data set (~~linked in main text Sec. 4)~~Kostadinov et al. (2022)). For more details see the scientific code used to do the uncertainty propagation (~~linked in main text Sec. 4~~Kostadinov et al. (2022)), as well as Kostadinov et al. (2016) and their Supplement.

S2   Modeled Backscattering Efficiencies

Example output phytoplankton Q_{bb} are plotted in Fig. S2A. For a fixed diameter, wavelength can significantly affect the values, especially at intermediate diameters. Coated sphere scattering patterns also exhibit spikes, the influence of which on computed IOPs is minimized here by having a high sampling frequency in diameter, D. Figure S2A also shows the Q_{bb} curves corresponding to the Gladstone-Dale (GD) equivalent homogeneous spheres. For most diameters, homogeneous spheres exhibit significantly lower backscattering efficiencies, which is consistent with prior studies (e.g. Bernard et al. (2009); Quirantes and Bernard (2006); Organelli et al. (2018)). This indicates that the contribution of phytoplankton to backscattering in the global ocean has likely been underestimated in previous studies (see Dall'Olmo et al. (2009)), in which homogeneous spheres were assumed for modeling of phytoplankton (e.g. Stramski and Kiefer (1991); Kostadinov et al. (2009)).

The difference between modeled phytoplankton and NAP Q_{bb} curves is shown in Fig. S2B. Unlike panel A, the curves here are band-averaged (see main text Sec. 2.2) and the median across all Monte Carlo runs is shown as an example. Note that NAP are modeled over a wider range of diameters as compared with phytoplankton. Phytoplankton represented as coated spheres still exhibit higher efficiencies than homogeneous NAP, but mostly only over the 1 to 10 µm diameter range. The difference here is driven by the choices of Mie inputs for phytoplankton vs. NAP. In particular, NAP are allowed to have a wider range of real RIs, accommodating possible contributions by minerogenic particles. Purely organic detrital NAP would have lower Q_{bb} than is shown in Supplementary Fig. S2B.

S3   Cumulative Backscattering Analysis

Here, we focus on investigating what particle size ranges contribute to the backscattering signal, which is investigated via cumulative b_{bp} plots (Fig. S4). Cumulative modeled b_{bp} curves for phytoplankton (Fig. S4A, 443 and 560 nm shown) indicate that, as expected, the higher the PSD slope, the larger fraction of the phytoplankton b_{bp} signal is due to the smallest phytoplankton cells. Generally, the 443 and 560 nm bands behave similarly, however, differences exist, e.g. at PSD slopes 3.5 and 4.0; specifically, at ξ=4.0, $\approx$60% of the signal is due to phytoplankton cells with $D < 3$ µm at 560 nm, whereas this value rises to $\approx$85% at 443 nm. A sigmoidal-like shape of this curve indicates that asymptotic values tend to be reached at low diameters and high diameters, i.e. most of the b_{bp} signal is captured within the range of D values used. Note that the size of the smallest photoautotroph - *Prochlorococcus* ($\approx$ 0.5 µm in diameter (Morel et al. (1993)) informs the choice of the lower diameter limit used for phytoplankton (Table 1).

Cumulative NAP b_{bp} for modeled spectra (Supplement Fig. S4B) indicates that for most PSD slopes, the size range used captures most of the signal, if NAP can be reasonably represented by homogeneous spheres. Importantly, for ξ=4.0, most of the signal comes from particles with D between 0.1 and 1.0 µm, and these smaller particles are also essential for reproducing modeled spectral shapes in the same range as observed satellite b_{bp} spectra. Coated spheres representing phytoplankton within their size range alone are not able to do so (not shown). This is an important observation, illustrating the need to better understand the nature of sub-micron particles (e.g. Stramski et al. (2004)). The difference between coated spheres and their Gladstone-Dale (GD) homogeneous equivalents in terms of cumulative b_{bp} (Fig. S4C) are a function of the differences in Q_{bb}

55 curve shapes (Fig. S2A) and the PSD slope used. At intermediate values of the PSD slope such as 4.0, $\approx 30\%$ of the signal is due to particles smaller than $D = 1.0$ µm in the case of coated spheres, whereas almost 60% of the signal is due to particles smaller than this threshold in the case of homogeneous spheres.

S4   PSD Validation Results: Further Discussion by Location

The PSD validation is briefly analyzed here further by location, taking a look first at all data except the in-line LISST data
60 from the NAAMES and EXPORTS cruises (Fig. S6A and B), and then the EXPORTS and NAAMES cruises in-line LISST data alone (Fig. S6C and D).

Fig. S6A illustrates that data from two specific locations are numerous and also likely drive the regression to a large degree - 1) the Plumes and Blooms (PnB) Project LISST data, which represents a coastal site, namely the Santa Barbara Channel in California, USA (SBC), and 2) the Equatorial Pacific (EqPac). While at SBC the satellite data underestimates PSD slopes, it
65 overestimates them at EqPac. Data from these locations tend to be clusters around specific ξ values, and these span a larger range in the satellite data, consistent with higher oligotrophy in the EqPac than in the SBC; the same is observed in the *in-situ* data, but to a lesser degree. Data from other various locations tend to span a wider *in-situ* range, which is captured by the satellite retrievals, albeit with substantial noise. With regards to N_0, inspection of the location-coded plot (Fig. S6B) indicates that a lot of the underestimated points come from the Equatorial Pacific clustered around *in-situ* $N_0 = 10^{15.75}$ m^{-4}; many
70 overestimated points are from the SBC.

Validation with the NAAMES and EXPORTS LISST data (Fig. S6C and D) adds a very significant number of matched-up points, compared to all the rest of the data, illustrating the value of in-line data collection. Validation regression slopes for these figures are quite similar to those for all the rest of the validation data, indicating a tendency for the satellite data to exhibit larger ranges and to overestimate values at the high end, and underestimate values at the low end, for both ξ and N_0. Importantly,
75 both regressions for the EXPORTS and NAAMES data appear to be driven by a cluster of points that is separate from the main another cluster of data. These main clusters are quite noisy and do not have a very large dynamic range. We note that these data come from the NAAMES 4 cruise for both ξ and N_0, and may not necessarily represent the same points. Importantly, the NAAMES 4 cruise is the only one of the four cruises that samples lower latitude, oligotrophic, open- ocean waters (Fig. S5B). This illustrates a limitation of the *in-situ* validation data - that its spatio-temporal coverage might be insufficient to
80 representatively sample the full dynamic range of the PSD parameters and/or to capture their global overall relationship.

S5   Details of Empirical Tuning Derivation

This section describes the details of the derivation of the N_O empirical tuning method. Monthly OC-CCI v5.0 imagery for years 2004 and 2015 (48 total images, 24 each for Chl and POC) were used to compute the PSD-derived Chl and POC. These values were then compared on a per-pixel basis against the standard OC-CCI v5.0 Chl product, and against the Stramski et al.
85 (2008) POC retrieval (termed the standard values here). These comparisons were used in an optimization procedure that finds

the best linear regression correction of the decimal logarithm of N_0. The cost function used was the average absolute value of the decimal logarithm of the ratio between the PSD-based and the standard values, summing the Chl and POC contributions and weighting them equally. This cost function is minimal when both Chl and POC standard and PSD-based retrievals are the same everywhere. The optimization was performed using the $\mathrm{Statistics\ and\ MachineLearning}^{\circledR}$ Toolbox of $\mathrm{MATLAB}^{\circledR}$. A hybrid optimization technique was implemented, using genetic algorithms (ga function) and the $\mathrm{fmincon}$ function. The optimization for each month returns one global value of linear slope and intercept to be applied to the original, un-tuned N_0 retrievals, in order to obtain the tuned retrievals (henceforth retrievals without tuning applied are referred to as "original"). The median of the 48 tuning slopes and intercepts thus obtained were subsequently used to adjust N_0 in log10 space as follows:

S6   Comparison with KSM09 Look-Up Tables

When the modeled b_{bp} spectra (main text Fig. 2A) are used to design look-up tables (LUTs) as in KSM09 (Kostadinov et al., 2009), one can compare the KSM09 algorithm to the model developed here. Results indicate that the LUTs relating the b_{bp} slope to the PSD slope are quite similar, differing by ≈ 0.2 (in PSD slope) at the most, when ξ values are from 3.5 to 4.0 (not shown). The LUTs practically coincide for very low and very high PSD slopes. LUTs of the new algorithm for the various sensors are very similar to each other. The LUTs linking the b_{bp} slope to the N_0 parameter for KSM09 and the new algorithm are also similar to first order (in logarithmic space). Importantly, the new algorithm LUTs (also nearly coinciding for the various sensors) indicate higher backscattering per particle for low b_{bp} slope values below ≈ 0.75 (typical for more eutrophic waters), and they indicate lower backscattering per particle for steeper backscattering spectral slopes (typical for more oligotrophic conditions). This can lead to up to a factor of ≈ 2 difference in retrieved N_0, i.e. in particle concentrations retrieved. This LUT difference leads to a reduction of the apparent range exaggeration of retrieved phyto C globally (low values in the subtropical gyres, and high values in the eutrophic areas). It is this range exaggeration that led to the need for the empirical tuning in Kostadinov et al. (2016). While the need for this tuning seems to persist for the new algorithm and is also implemented here (Sec. S5), validation and comparisons results here suggest that for some variables and algorithms being compared with, the original version of the novel PSD/phyto C algorithm performs better.
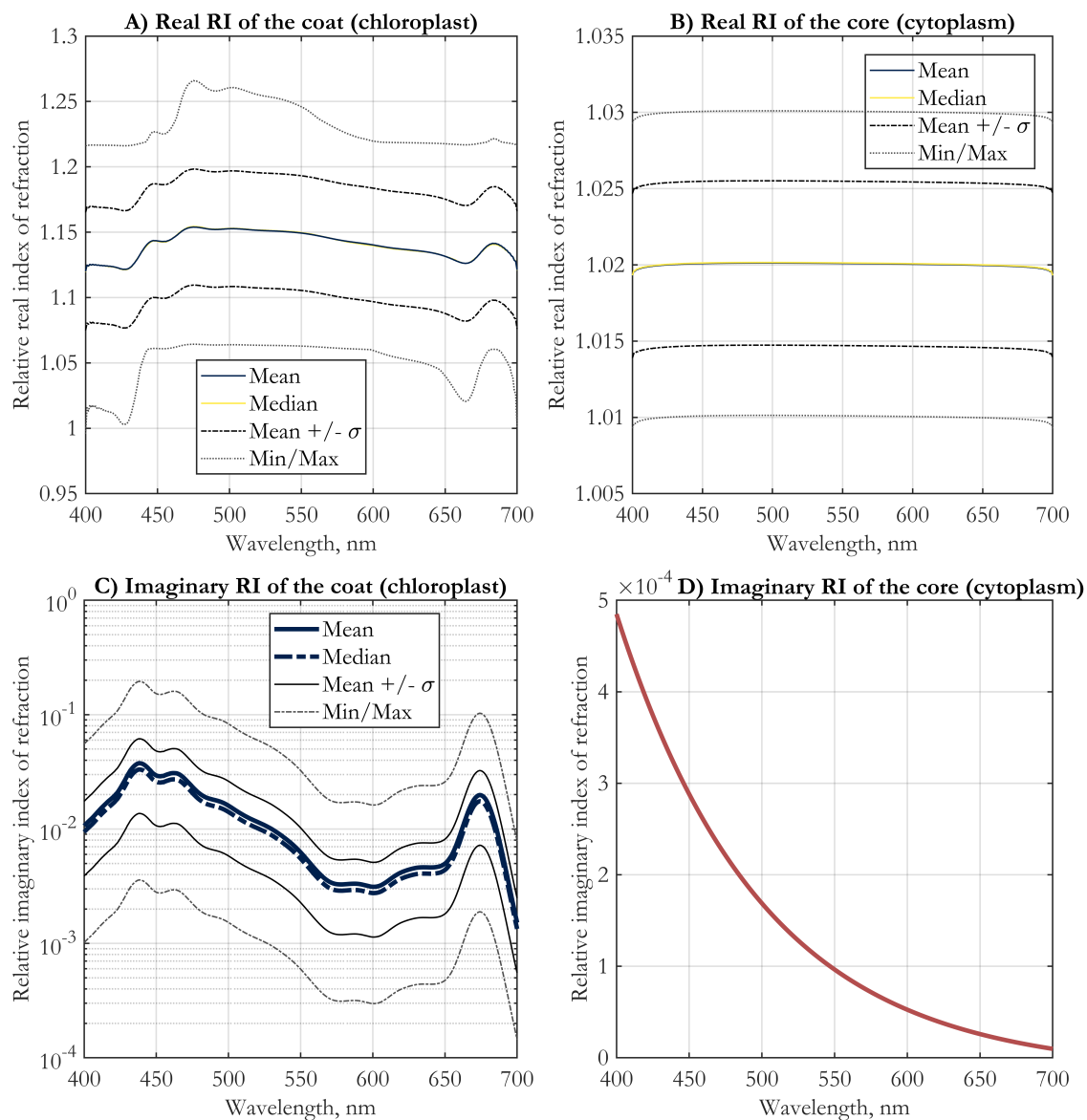
Figure S1. EAP-based hyperspectral complex refractive index (RI) inputs to the coated spheres (representing phytoplankton cells) Mie code, given relative to the index of refraction of seawater: A) real RI of the coat as chloroplast, B) real RI of the core as cytoplasm, C) imaginary RI of the coat as chloroplast, and D) imaginary RI of the core as cytoplasm. In panel A, the mean and median curves almost coincide. For panels A-C, the statistics of the input distributions used in the Monte Carlo simulation are given, namely mean, median, mean plus and minus one standard deviation, and the minimum and maximum values. Panels A and B exhibit spectral dependencies according to the Kramers-Kronig relations.
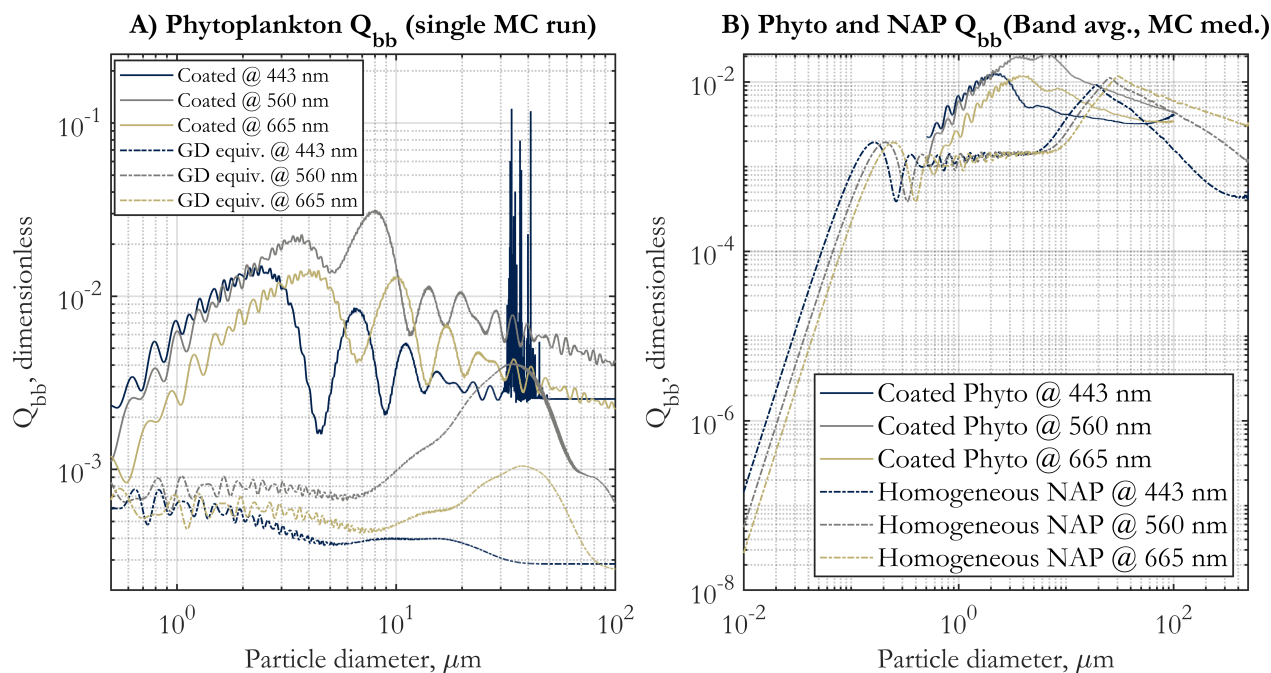
Figure S2. (A) Example backscattering efficiencies, Q_{bb}, for phytoplankton modeled as coated spheres. A single Aden-Kerker computation run is shown, using the median inputs from the Monte Carlo simulations. The coated sphere results for three different wavelengths (corresponding to OLCI nominal bands and ~~the~~ OC-CCI v5.0 data set bands; color coded as in legend) are shown as solids lines. The corresponding Gladstone-Dale (GD) - equivalent homogeneous sphere results are shown in dash-dot lines. (B) Band-averaged backscattering efficiencies, $\overline{Q_{bb}}$, for phytoplankton modeled as coated spheres (solid lines) and NAP modeled as homogeneous spheres (dash-dot lines). The median values across all Monte Carlo simulation runs are shown.
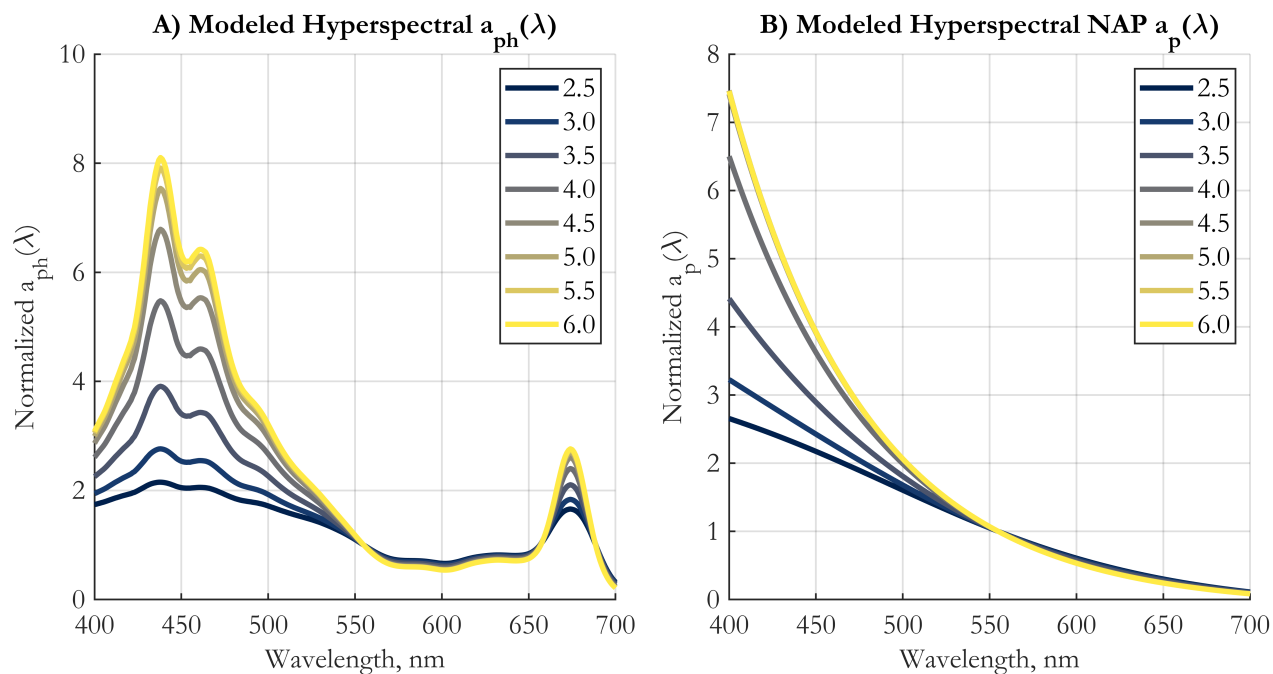
Figure S3. Modeled hyperspectral particulate absorption coefficient by (A) phytoplankton, $a_\phi(\lambda)$, using EAP-based coated spheres Mie scattering computations, and (B) NAP, $a_{NAP}(\lambda)$, modeled as homogeneous spheres, as a function of the input power-law PSD slope (color-coded solid lines, as in legend). All spectra are shown normalized to the respective values at 555 nm.
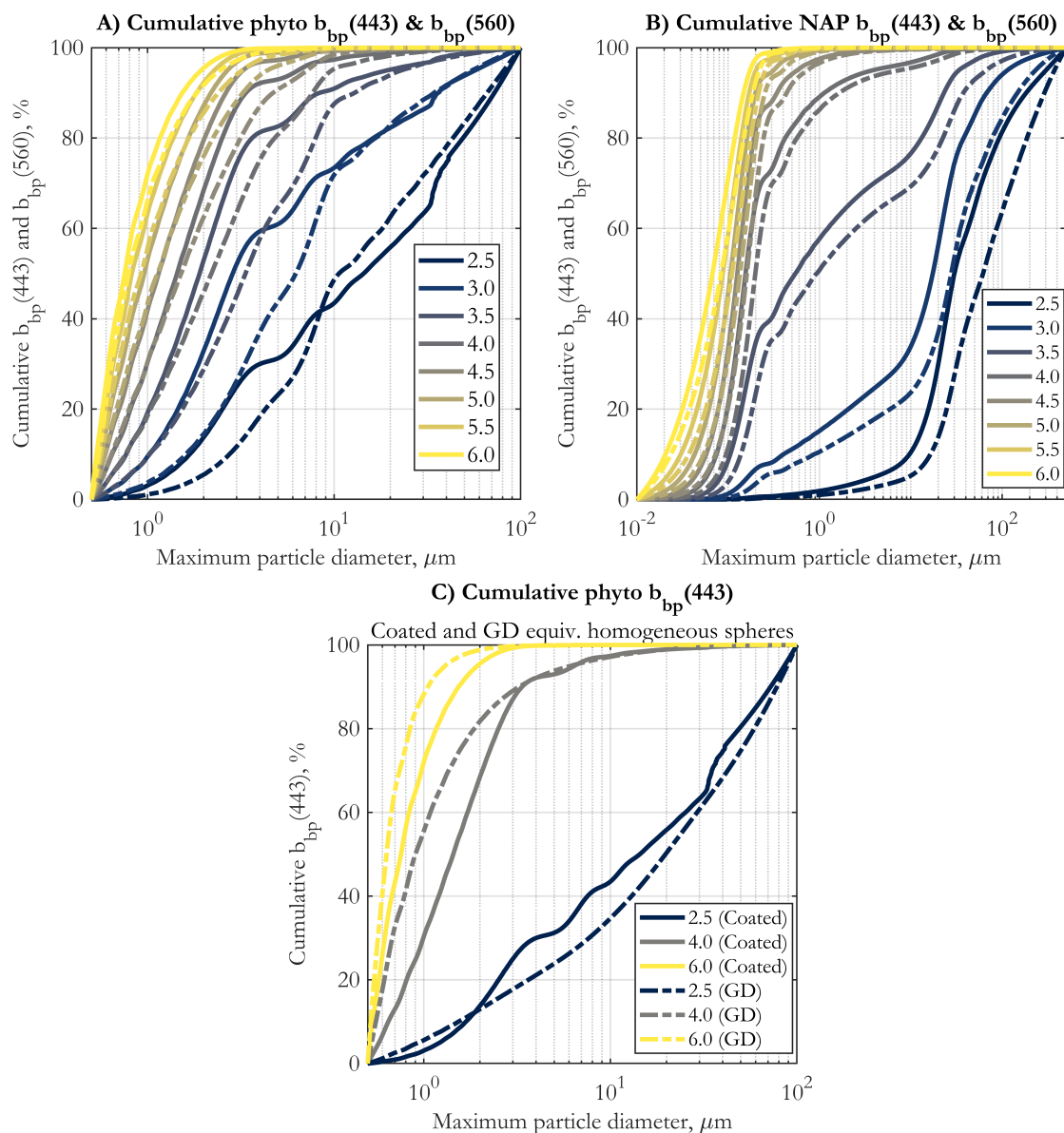
Figure S4. Cumulative $b_{bp}(443)$ (solid lines) and $b_{bp}(560)$ (dash-dot lines) for phytoplankton (A) and NAP (B) as a function of PSD slope ξ (color coded as in legend). For each particle diameter (x-axes) the plots show the percentage of backscattering due to particles smaller than or equal to that diameter (y-axes). (C) Cumulative $b_{bp}(443)$ for phytoplankton modeled as coated spheres (solid lines) and for the corresponding Gladstone-Dale (GD) equivalent homogeneous spheres (dash-dot lines). Curve pairs are shown for three different PSD slopes ξ, namely 2.5, 4.0 and 6.0 (color coded as in legend). All panels display results of the single forward illustrative Mie calculation run which uses medians of the Monte Carlo varied inputs.
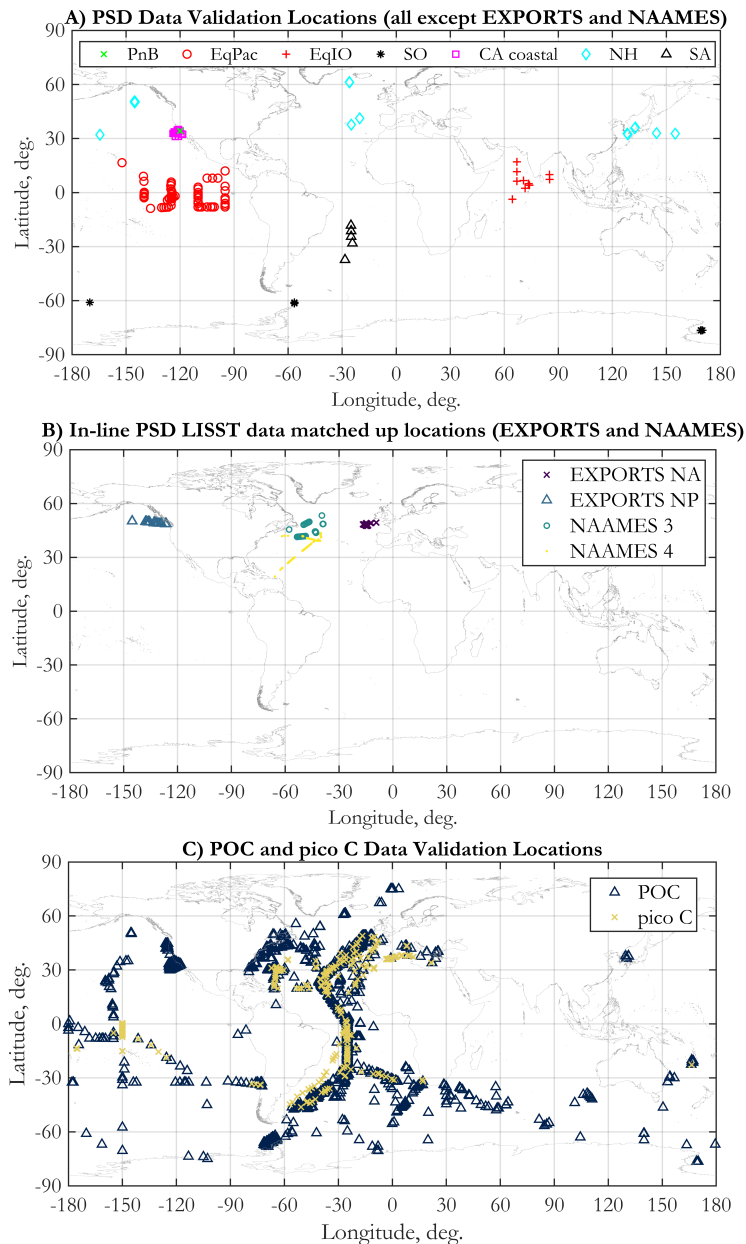
Figure S5. A) Locations of *in-situ* PSD data used in algorithm validation, other than those from the EXPORTS North Atlantic (NA), EXPORTS North pacific (NP) and NAAMES 3 and NAAMES 4 cruises. Different regions are shown using symbols as in the legend, in which acronyms are as follows - Plumes and Blooms Project (PnB), Equatorial Pacific (EqPac), Equatorial Indian Ocean (EqIO), Southern Ocean (SO), CA coastal areas excluding PnB (CA coastal), Northern Hemisphere higher latitudes (NH), and Southern Atlantic (SA). B) In-line LISST PSD data used in algorithm validation, from the EXPORTS North Atlantic (NA), EXPORTS North Pacific (NP) and NAAMES 3 and NAAMES 4 cruises (as in legend). C) Locations of *in-situ* data used in validation match-ups for ~~all variables, as shown in the legend -~~ particulate organic carbon (POC, ~~green~~ blue triangle), and pico-phytoplankton carbon (pico C, ~~red~~ yellow 'x'). In all three panels, ~~and PSD~~ only locations for which a valid match-up is available (~~blue dot~~and used in the validation presented here) are shown.
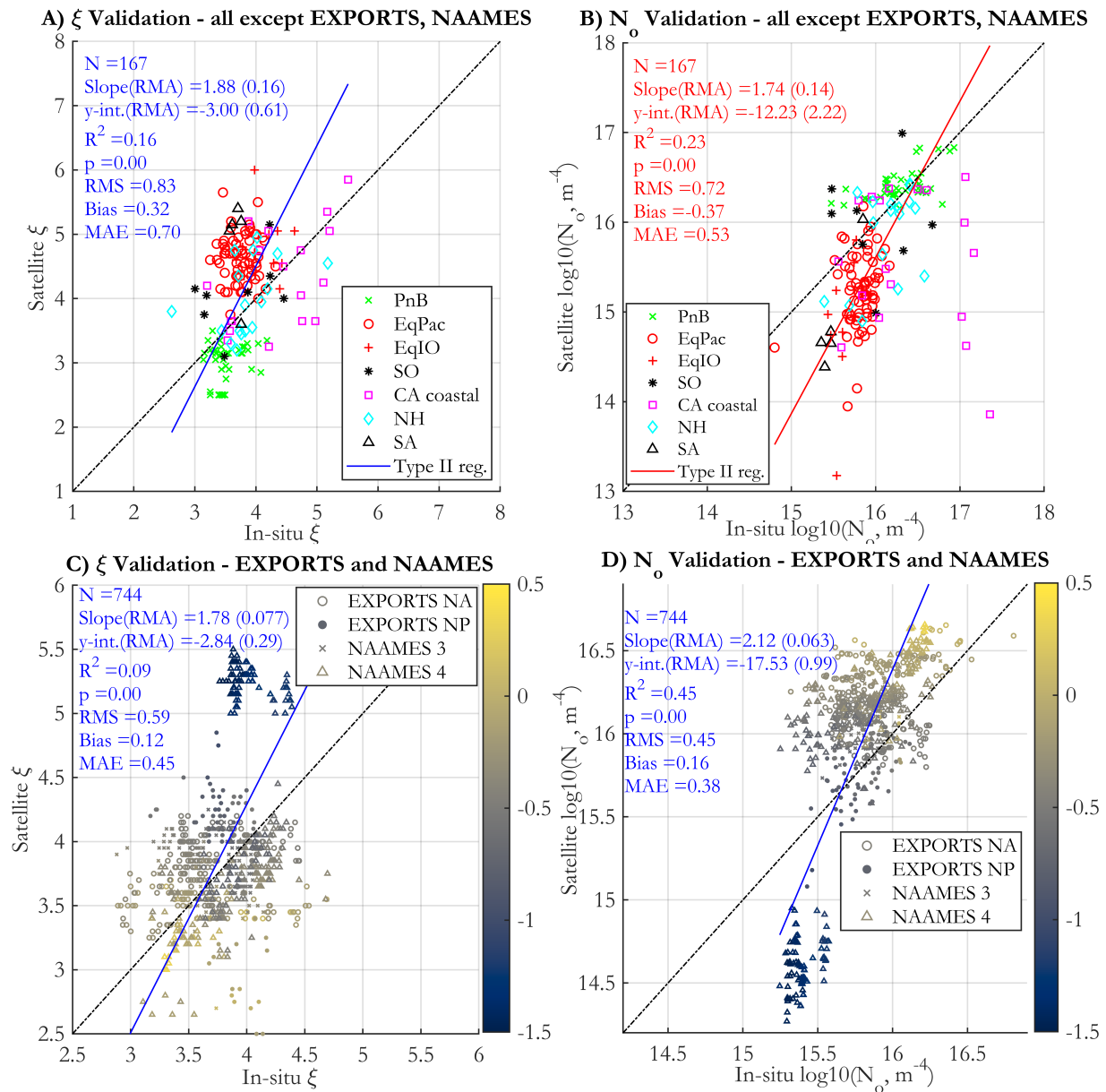
Figure S6. (A) The same validation regression as in main text Fig. 8A, but only data *not* coming from the EXPORTS and NAAMES cruises in-line LISST measurements are plotted, and the points are color and symbol coded according to geographic area, as follows: Plumes and Blooms project (e.g. Toole and Siegel (2001); Kostadinov et al. (2007)) (PnB, green 'x'); Equatorial Pacific (EqPac, red circles); Equatorial Indian Ocean (EqIO, red '+'); Southern Ocean (SO, black '*'); California (CA) coastal area (purple squares); higher latitude Northern Hemisphere points (> 30° latitude, NH, cyan diamonds), and South Atlantic (SA, black triangles); (B) same as in panel A, but for the N_0 parameter (axes in log10 space). (C) Same as in panel A, but for the in-line LISST measurements from the EXPORTS and NAAMES cruises, as in the legend (NA = North Atlantic, NP = North Pacific). Points are color-coded according to satellite chlorophyll-a retrievals (from the OC-CCI v5.0 match-ups), as in the colorbar (log-10 scale in mg m^{-3}). (D) Same as in panel C, but for the N_0 parameter (axes in log10 space).
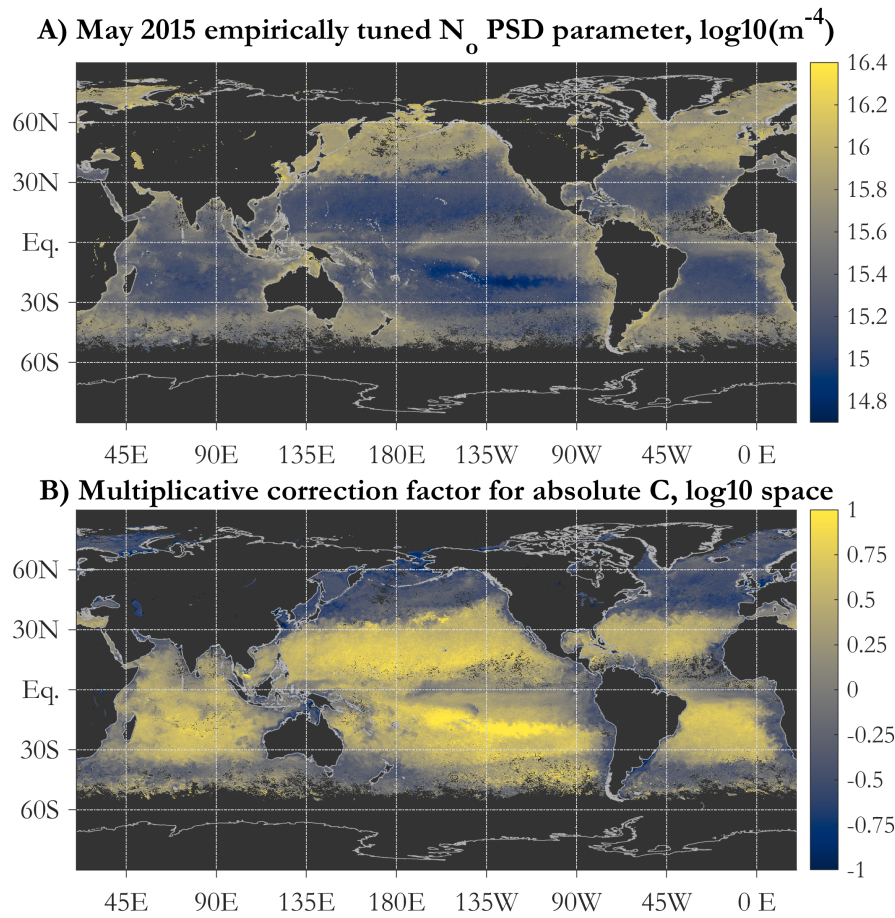
Figure S7. (A) The N_0 parameter (m^{-4}, mapped in log10 space) after tuning has been applied (main text Eq. 7) in order to achieve more realistic global estimates of POC and Chl via the PSD model presented here; (B) A multiplicative tuning factor (dimensionless) to be applied to absolute carbon (and Chl) estimates from the PSD-based algorithm; the factor is applied in linear space, but it is plotted in log10 space, i.e. a map value of 0 indicates a tuning factor of 1, meaning that the tuned and original values are the same. Both panels use the monthly OC-CCI v5.0 data for May 2015 as input.
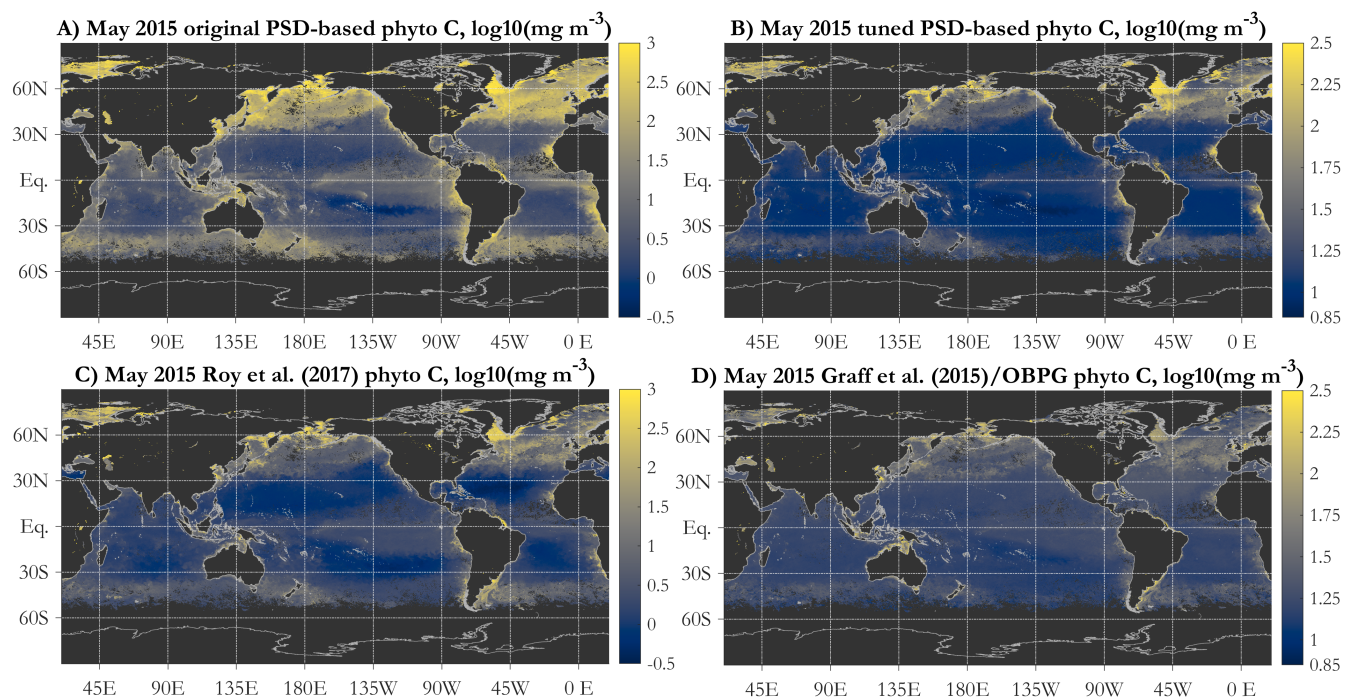
Figure S8. (A) Original PSD-based phyto C, same as main text Fig. 4A; (B) Tuned PSD-based phyto C; (B) The Roy et al. (2017) absorption-based and PSD-based phyto C retrieval, and (C) the Graff et al. (2015) phyto C retrieval, based on a scaling of b_{bp}. All three panels use the monthly OC-CCI v5.0 data for May 2015 as input. Note the different color scale of panels A and C vs. panels B and D.
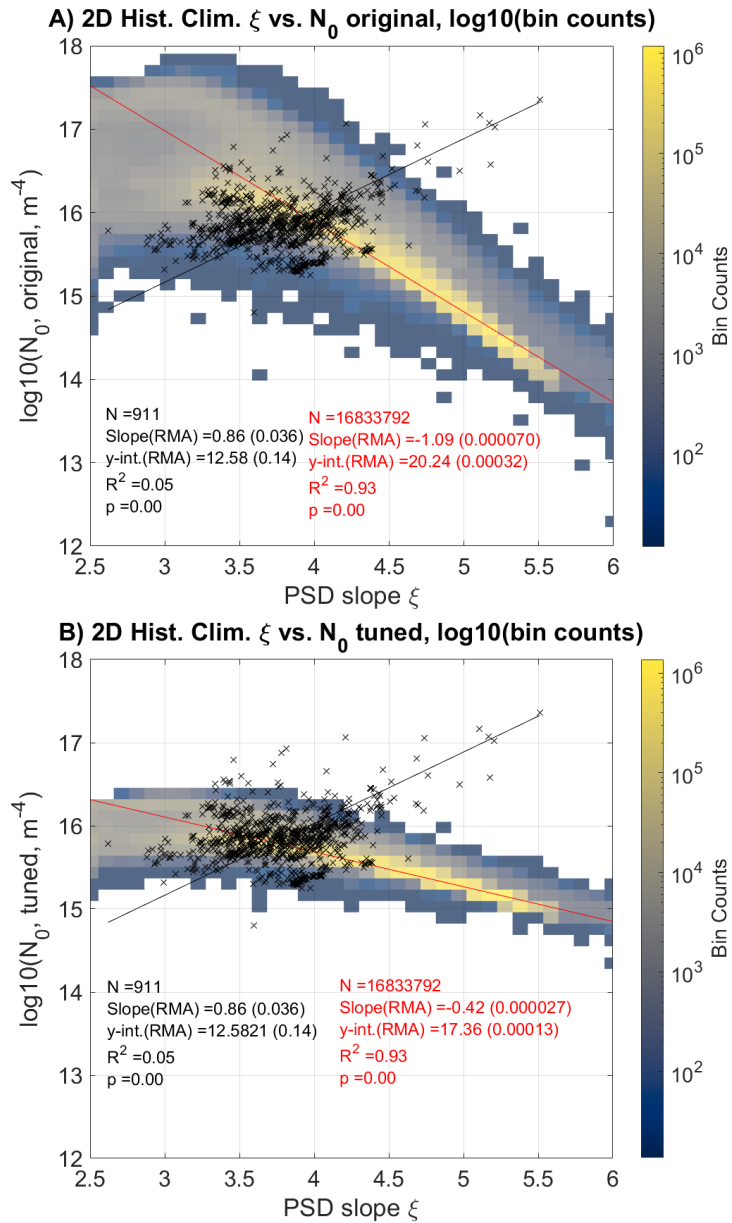
Figure S9. A 2D histogram of the PSD slope ξ vs. the N_0 parameter. The overall climatological PSD parameters images Kostadinov et al. (2022) from the OC-CCI_v5.0_data_set (Sathyendranath et al. (2021)) were used for these histograms, in sinusoidal projection. Panel A uses the original (not tuned) N_0 parameter, and panel B uses the tunes N_0. The climatological satellite data histogram is overlaid with a scatter plot of the matched-up *in-situ* data used in the validation. Type II least squares regression lines through both satellite and *in-situ* data are shown, with regression statistics printed. The satellite data regression line and statistics are red, with N = 16,833,792 and the line is with a negative slope. The *in-situ* data regression line is with a positive slope and black, and its associated statistics is printed in black, with N = 911.

Figure S10. A 2D histogram of the PSD slope ξ vs. the N_0 parameter. The overall climatological PSD parameters images Kostadinov et al. (2022) from the OC-CCI v5.0 data set (Sathyendranath et al. (2021)) were used for these histograms, in sinusoidal projection. Panel A uses the original (not tuned) N_0 parameter, and panel B uses the tunes N_0. The climatological satellite data histogram is overlaid with a scatter plot of the matched-up *in-situ* data used in the validation. Type II least squares regression lines through both satellite and *in-situ* data are shown, with regression statistics printed. The satellite data regression line and statistics are red, with N = 16,833,792 and the line is with a negative slope. The *in-situ* data regression line is with a positive slope and black, and its associated statistics is printed in black, with N = 911.

S14

110 References

Bernard, S., Probyn, T. A., and Quirantes, A.: Simulating the optical properties of phytoplankton cells using a two-layered spherical geometry, Biogeosciences Discussions, 6, 1497–1563, https://doi.org/10.5194/bgd-6-1497-2009, 2009.

Dall'Olmo, G., Westberry, T. K., Behrenfeld, M. J., Boss, E., and Slade, W. H.: Significant contribution of large particles to optical backscattering in the open ocean, Biogeosciences, 6, 947–967, https://doi.org/10.5194/bg-6-947-2009, 2009.

115 Graff, J. R., Westberry, T. K., Milligan, A. J., Brown, M. B., Dall'Olmo, G., van Dongen-Vogels, V., Reifel, K. M., and Behrenfeld, M. J.: Analytical phytoplankton carbon measurements spanning diverse ecosystems, Deep-Sea Research Part I: Oceanographic Research Papers, 102, 16–25, https://doi.org/10.1016/j.dsr.2015.04.006, 2015.

Kostadinov, T., Siegel, D., Maritorena, S., and Guillocheau, N.: Ocean color observations and modeling for an optically complex site: Santa Barbara Channel, California, USA, Journal of Geophysical Research: Oceans, 112, https://doi.org/10.1029/2006JC003526, 2007.

120 Kostadinov, T., Siegel, D., and Maritorena, S.: Retrieval of the particle size distribution from satellite ocean color observations, Journal of Geophysical Research: Oceans, 114, https://doi.org/10.1029/2009JC005303, 2009.

Kostadinov, T., Milutinovic, S., Marinov, I., and Cabré, A.: Carbon-based phytoplankton size classes retrieved via ocean color estimates of the particle size distribution, Ocean Science, 12, https://doi.org/10.5194/os-12-561-2016, 2016.

Kostadinov, T. S., Roberston-Lain, L., Bernard, S., Zhang, X., and Loisel, H.: PSD_PhytoC_v2021: Ocean Color Algorithm for the Re-
125 trieval of the Particle Size Distribution and Size-Partitioned Phytoplankton Carbon: Algorithm Development and Operational Code, https://doi.org/10.5281/zenodo.6354654, 2022.

Kostadinov, T. S., Robertson-Lain, L., Kong, C. E., Zhang, X., Maritorena, S., Bernard, S., Loisel, H., Jorge, D. S. F., Kochetkova, E., Roy, S., Jönsson, B., Martinez-Vicente, V., and Sathyendranath, S.: Particle Size Distribution and Size-partitioned Phytoplankton Carbon Using a Two-Component Coated-Spheres Bio-optical Model: Monthly Global 4 km Imagery Based on the OC-CCI v5.0 Merged Ocean Color
130 Sat, https://doi.org/10.1594/PANGAEA.939863, 2022.

Menden-Deuer, S. and Lessard, E. J.: Carbon to volume relationships for dinoflagellates, diatoms, and other protist plankton, Limnology and Oceanography, 45, 569–579, https://doi.org/10.4319/lo.2000.45.3.0569, 2000.

Morel, A., Yu-Hwan Ahn, Partensky, F., Vaulot, D., and Claustre, H.: Prochlorococcus and Synechococcus: a comparative study of their optical properties in relation to their size and pigmentation, Journal of Marine Research, 51, 617–649,
135 https://doi.org/10.1357/0022240933223963, 1993.

Organelli, E., Dall'Olmo, G., Brewin, R. J., Tarran, G. A., Boss, E., and Bricaud, A.: The open-ocean missing backscattering is in the structural complexity of particles, Nature Communications, 9, https://doi.org/10.1038/s41467-018-07814-6, 2018.

Quirantes, A. and Bernard, S.: Light-scattering methods for modelling algal particles as a collection of coated and/or nonspherical scatterers, Journal of Quantitative Spectroscopy and Radiative Transfer, 100, 315–324, https://doi.org/10.1016/j.jqsrt.2005.11.048, 2006.

140 Roy, S., Sathyendranath, S., and Platt, T.: Size-partitioned phytoplankton carbon and carbon-to-chlorophyll ratio from ocean colour by an absorption-based bio-optical algorithm, Remote Sensing of Environment, 194, 177–189, https://doi.org/10.1016/j.rse.2017.02.015, 2017.

Sathyendranath, S., Jackson, T., Brockmann, C., Brotas, V., Calton, B., Chuprin, A., Clements, O., Cipollini, P., Danne, O., Dingle, J., Donlon, C., Grant, M., Groom, S., Krasemann, H., Lavender, S., Mazeran, C., Mélin, F., Müller, D., Steinmetz, F., Valente, A., Zühlke, M., Feldman, G., Franz, B., Frouin, R., Werdell, J., and Platt, T.: ESA Ocean Colour Climate Change Initiative (Ocean_Colour_cci):
145 Version 5.0 Data. NERC EDS Centre for Environmental Data Analysis, https://doi.org/10.5285/1dbe7a109c0244aaad713e078fd3059a, 2021.

Stramski, D. and Kiefer, D. A.: Light scattering by microorganisms in the open ocean, Progress in Oceanography, 28, 343–383, https://doi.org/10.1016/0079-6611(91)90032-H, 1991.

150 Stramski, D., Boss, E., Bogucki, D., and Voss, K. J.: The role of seawater constituents in light backscattering in the ocean, Progress in Oceanography, 61, 27–56, https://doi.org/10.1016/j.pocean.2004.07.001, 2004.

Stramski, D., Reynolds, R. A., Babin, M., Kaczmarek, S., Lewis, M. R., Röttgers, R., Sciandra, A., Stramska, M., Twardowski, M. S., Franz, B. A., and Claustre, H.: Relationships between the surface concentration of particulate organic carbon and optical properties in the eastern South Pacific and eastern Atlantic Oceans, Biogeosciences, 5, 171–201, https://doi.org/10.5194/bg-5-171-2008, 2008.

Toole, D. A. and Siegel, D. A.: Modes and mechanisms of ocean color variability in the Santa Barbara Channel, Journal of Geophysical

155 Research: Oceans, 106, 26 985–27 000, https://doi.org/10.1029/2000JC000371, 2001.